Université de Montréal

The Dynamics of Sustained Reentry in a Loop Model with Discrete Gap Junction Resistance

Par

Wei Chen

Institute de génie biomédical

Faculté de médecine

Mémoire présenté à la Faculté des études supérieures

en vue de l'obtention du grade de Maîtrise ès sciences appliquées

en génie biomédical

Avril 2007

Université de Montréal

Faculté des études supérieures

Ce mémoire intitulé:

The Dynamics of Sustained Reentry in a Loop Model with Discrete Gap Junction Resistance

présenté par:

Wei Chen

a été évalué par un jury composé des personnes suivantes:

A. Robert LeBlanc, Ing., D.Sc.A

président-rapporteur

Alain Vinet, Ing., Ph.D.

directeur de recherche

Jacques Bélair, Ph.D.

membre du jury

Résumé

Lors d'un battement cardiaque normal, l'activation électrique débute dans le nœud sinusal et se propage dans les deux oreillettes. Elle atteint ensuite le faisceau de His, puis finalement les fibres de Purkinje qui distribuent l'excitation dans les ventricules pour déclencher la contraction. Cette propagation se produit parce que les myocytes cardiaques peuvent produire un potentiel d'action quand ils sont dépolarisés au-delà d'un seuil. Parce que les cellules sont connectées électriquement, la dépolarisation d'une partie du tissu cardiaque provoque une augmentation du potentiel dans le tissu voisin, jusqu'à ce que ce dernier atteigne son seuil d'excitation et devienne à son tour une source qui permet à la propagation de se poursuivre.

Les propriétés électriques de la membrane des myocytes cardiaques ventriculaires ont été décrites par différents modèles mathématiques. Dans ce travail, nous utilisons une variante du modèle de Beeler et Reuter, qui fournit une représentation de type Hodgkin-Huxley des conductances de courants ioniques membranaires. En voltage imposé, le modèle est constitué par un système d'équations différentielles ordinaires qui décrivent la dynamique temporelle du potentiel membranaire, des variables portes contrôlant la conductance des différents canaux ioniques et de la concentration interne de calcium. Pour ce qui est de la description du tissu ventriculaire, la plupart des travaux de modélisation considèrent la membrane et les milieux intra et extracellulaires comme continus, de telle sorte que les flux de courants à travers la membrane et les milieux résistifs intra et extracellulaires sont représentés par une équation aux dérivées partielles. Cependant, le tissu cardiaque est constitué par des myocytes discrets, dont les milieux intracellulaires sont joints par des protéines. Ces dernières agissent comme des résistances connectant électriquement les milieux intracellulaires des cellules voisines. C'est ce dernier point de vue que nous avons adopté dans cet mémoire.

Le but de notre étude est d'examiner l'effet des résistances de jonction sur les caractéristiques des réentrées pouvant se produire dans un modèle de boucle unidimensionnelle de cellules cardiaques. La réentrée cardiaque correspond à la propagation soutenue

d'un front d'activation autour d'un obstacle anatomique ou fonctionnel. La propagation autour d'une boucle unidimensionnelle est donc le modèle de réentrée le plus simple. Des travaux précédents sur des boucles uniformes et continues, dont les propriétés membranaires étaient représentées par divers modèles ioniques, ont montré que la réentrée pouvait demeurer soutenue mais devenir quasi-périodique quand la dimension de la boucle était inférieure à une longueur critique L_{crit} et qu'elle s'interrompait pour des longueurs inférieures à une longueur minimale L_{min}. Ces travaux ont montré que la transition de réentrée périodique à réentrée quasi-périodique était contrôlée par les courbes de restitution et de dispersion, décrivant respectivement la variation de la durée des potentiels d'action et de la vitesse de propagation en fonction de la prématurité de la stimulation. Nous avons étudié une boucle formée de cellules discrètes liées par des résistances de jonction et avons développé une méthode numérique pour solutionner le système de réaction-diffusion décrivant ce milieu. Nous avons trouvé que la diminution de L_{crit} et de L_{min} résultant de l'augmentation des résistances de jonction n'était pas réductible à un simple facteur d'échelle appliqué sur les résultats des boucles uniformes continues. Nous avons plutôt montré que les résultats étaient expliqués par les changements dans les courbes de restitution et de dispersion induits par l'effet des résistances de jonction sur la dynamique locale.

Mots clé : Potentiel d'action, Réentrée, Réentrée stable périodique et quasi-périodique, Résistance de jonction, Bifurcation, Durée de potentiel d'action, Intervalle diastolique, Longueur de boucle, Temps de conduction, Vitesse de conduction, Mode-0, Mode-1.

Abstract

In a normal heartbeat, electrical activation starts from the SA node and propagates to both atria. It travels successively through the AV node, the His Bundle and finally the Purkinje fibers that distribute the excitation and contract ventricles.

The electrical activation is formed by the unequal ionic distribution on both sides of the sarcoplasmic membrane, producing a difference of potential between the intra and extracellular media. The electrical properties of the ventricular cardiac myocytes are described by the different mathematical models. The Hodgkin-Huxley model and Beeler-Reuter model use the ordinary differential equation to simulate membrane potential as a time-dependent function. The bifurcation phenomena of action potential duration and diastolic interval are simulated, which are proved by the finite difference model.

The action potential propagates in cardiac tissue. The low-dimensional model was employed. In the one-dimensional model, since cardiac tissue is regarded as the uniform continuous cable, bifurcation phenomena are simulated, and these results are proven by the integral delay model. The other model is that the gap junction resistance exists between cells. The propagation delay is shown between cells. The action potential propagates in the one-dimensional ring with the gap junction resistance, shown to be the most interesting in recent research.

The purpose of our study is to investigate the effect of gap junction resistance on the characteristics of reentry in a one-dimensional ring of model cardiac tissue. Tachyarrhythmia is commonly induced by reentry. Cardiac reentry corresponds to the self-sustained propagation of an activation front around a functional or anatomical obstacle. Propagation around a one-dimensional ring is the simplest model of reentry. Previous work on a uniform continuous 1-D ring model, with membrane properties represented by an ionic model, has shown that reentry was still sustained but quasiperiodic, below a critical length L_{crit}, and that it was blocked for rings shorter than a minimum length L_{min}. The transition from periodic to

quasiperiodic reentry was shown to be controlled by the restitution and dispersion curves, giving respectively the action potential duration and speed of propagation as a function of prematurity. However, cardiac myocytes are connected by discrete channels, called gap junctions, acting as resistance between the cells. We have studied a ring of cells connected by discrete gap resistances (R) and developed a numerical method of solving the resulting reaction-diffusion system. We found that the decrease of L_{crit} and L_{min} as a function of R was not a simple scaling of the results of the uniform ring, but could be explained by the change in the restitution and dispersion curves induced by the resistance that modulates the effect of neighbors on the local dynamics.

Keywords: Action potential, Reentry, Stable Reentry, Quasiperiodic reentry, Gap junction resistance, Bifurcation, Action potential duration, Diastolic interval, Ring length, Conduction time, Conduction velocity, Mode-0, Mode-1.

Contents

List of Tables

List of Figures

List of Symbolic Abbreviations

A or APD	Action potential
A_e	Area of extracellular membrane
A_i	Area of intracellular membrane
ATP	Adenosine triphosphate
AV	Atrioventricular
α	Rate constant of dynamic value
β	Rate constant of dynamic value
BCL	Basic cycle length
BR	Beeler-Reuter
Ca	Calcium
$[Ca]$	Concentration of calcium
Cl	Chlorine
C_m	Membrane capacity
ct	Conduction time
D or DIA	Diastolic interval
E_{Na}	Sodium Nernst potential
E_{Ca}	Calcium Nernst potential
i_{Ca}	Current of calcium
I_{ext}	External current
i_{K1}	Time-independent potassium current
i_{Na}	Current of sodium

i_{x1}	Time-dependent potassium current
I_{thr}	Threshold current of exciting membrane
K	Potassium
L	Ring length
λ_n	Wave length
L_c	Cell length
L_{crit} or X_{crit}	Critical ring length
L_{min} or X_{min}	Minimal ring length
MBR	Modified Beeler-Reuter
$M-0$	Mode-0
$M-1$	Mode-1
Na	Sodium
QP	Quasiperiod
R or r_g	Gap junction resistance
SA	Sinoatrial
τ_y	Time constant of dynamic value
θ or $Theta$	Conduction velocity
V or V_m	Membrane potential
V_e	Extracellular potential
V_i	Intracellular potential
VT	Ventricular Tachycardias
y	Dynamic value

Acknowledgments

First of all I would like to express my sincere gratitude to Professor Alain Vinet for his continual encouragement, for his warm-hearted guidance, for his helpful comments and discussions. Without his cordial support, this work would have never taken place. I am very honoured to begin my scientific career under his guidance.

I am also grateful to Dr. YaLin Yin, Dr. Mark Potse, Mr. Louis-Philippe Richer and Mr. Feng Xiong, for their useful comments and discussion.

The numerical calculations were performed using the PC at the Research center of Hôpital du Sacré-Cœur at Université de Montréal.

Finally, I would like to thank the CNRSG for providing financial support during my master's course.

Chapter 1

Introduction

In Canada and the USA, cardiovascular diseases remained the main cause of death in 2003, being respectively responsible (rate per 100,000 population) for 133.3 [1] and 232.3 [2] deaths in these two countries. Cardiac Rhythm disorders lead to over 400,000 cases of sudden death annually in the USA alone [3]. Reentry, which refers to the self-sustained propagation of an activation front in the cardiac tissue, is one of the major mechanisms causing cardiac arrhythmia [4–8]. Understanding the effect of the ionic and structural properties of the tissues at the onset and perpetuation of reentry could thus be useful in designing more appropriate prophylactic or curative interventions. The purpose of our study is to investigate the effect of intercellular gap junction resistance on the characteristics of reentry in one-dimensional ring of model cardiac tissue.

1.1 Membrane Potential

In the cardiac myocyte, there are high concentrations of intracellular potassium (K^+) inside the cell while the concentrations of sodium (Na^+), chloride (Cl^-), and calcium (Ca^{2+}) are less than in the extracellular fluid [9–11]. The unequal ionic distribution on both sides of the sarcoplasmic membrane produces a difference of potential between the intra and extracellular media. Ions can cross the membrane through channels that are specific to each ionic species. The movement of the ions across the channels is driven by both the gradient of concentration specific to each species and the gradient of the potential resulting from the whole population

of ions. In addition, pumps such as the ATP-driven $Na - K$ exchanger can move the ions against their electrochemical potentials and can restore or maintain the gradients of concentration.

In the resting state, the membrane is much more permeable to K^+, such that the resting membrane potential ($V_m = V_{in} - V_{out}$) is close to the K^+ reversal potential given by the Nernst equation [9–11]:

$$V_m = \frac{RT}{F} ln(\frac{K_0}{K_i}) \approx -90mV \ \ at \ T = 300K \tag{1.1}$$

When a myocyte is depolarized by the effect of neighbouring excited cells or an external stimulus raising the potential over a threshold value ($\sim -50mV$) [9–11], the sodium channels open and give a transient inward current that brings V_m close to the Na reversal potential [9–11]. Because this phase does not depend on a current provided by an external source, it is called a regenerative or active membrane response. The fast Na-driven increase of potential is called the upstroke. This increase in sodium permeability is transient, and within a few milliseconds it is markedly curtailed. At the end of the upstroke, the sodium permeability of the membrane diminishes to a level near that of the resting state. However, the membrane potential does not return to the resting potential. It is maintained near zero for a period before it repolarizes. This long lasting depolarized phase is called the plateau. The plateau is caused by the opening of the Ca channels that lets the calcium ion flow inward. This calcium current is often referred to as the slow current to distinguish it from the rapid sodium current. It is the calcium inflow, that triggers the release of calcium for the sarcoplasmic reticulum, which is important in the contractile response. At a later time, the calcium channels begin to close as the K channels start to open, which ends the plateau stage and initiates the final repolarizing phase of the action potential. The plateau is important because it delays repolarization. Since the cardiac cell cannot be excited again until it has repolarized to negative potential below the threshold level ($-50mV$), the plateau defines a long absolute refractory period, the period of inexcitability following an excitation. The duration of the action potential of ventricular myocardial cell is approximately $250ms$ in large mammals [9].

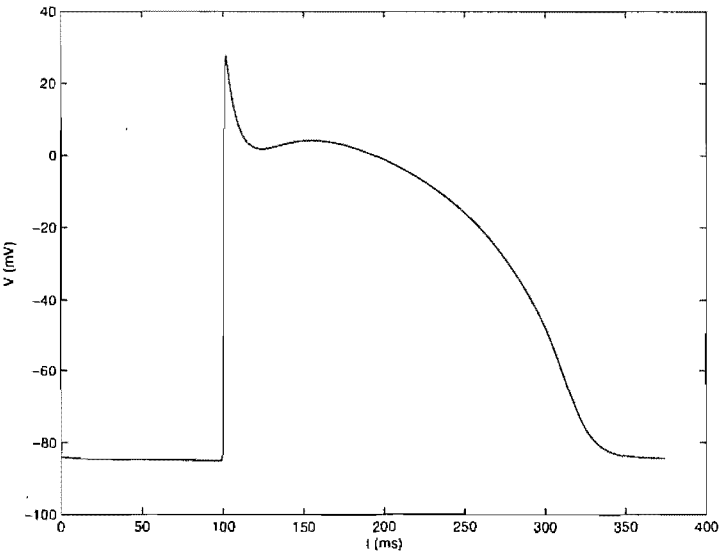

Figure 1.1: Schematic diagram of transmembrane action potential for ventricular cell.

The schematic diagram of the action potential is given by Fig. 1.1.

In normal cardiac cells, refractoriness is primarily controlled by the membrane potential. The absolute refractory period coincides with the period when the membrane potential is more positive than the threshold potential. The relative refractory period, in which a higher stimulation current has to be applied to launch an action potential, corresponds fairly closely to the phase of repolarization when the membrane potential is between the threshold potential and the resting potential. In some cardiac cells, the relative refractory period is followed by a supernormal period of enhanced excitability near the termination of repolarization. The excitability of cardiac cells, assessed by applying electrical stimuli, has received considerable alteration. The strength, duration, and polarity of the applied current are all important in determining responses. In general, the longer the duration of the stimulus, the less the intensity of current is required for excitation. For a fixed stimulus duration, the minimal stimulus required to produce an action potential is referred to as the stimulus threshold. The relationship between current strength and duration for threshold stimuli is approximately hyperbolic. Certain cardiac cells, such as cells of the sinoatrial (SA) node, spontaneously depolarize to threshold potential to generate action potentials. Generally,

such automatic cells exist in the sinoatrial node, the atrioventricular (AV) node, the His bundle and the peripheral Purkinje network. There is considerable functional heterogeneity among these components; however, each has properties of automaticity and/or conduction that differentiate it from ordinary working myocardial cells.

1.2 Rhythmical Excitation of the Heart

In a normal beat, electrical activation starts from the SA node which propagates to both atria. It travels successively through the AV node, the His Bundle and finally to the Purkinje fibers that distribute the excitation around both ventricles [9–11]. In human, when the system functions normally, the atria contract about one sixth of a second ahead of the ventricles, which allows the final filling of the ventricles before they pump the blood through whole body [10, 12]. Another especially important property of the system is that it allows all the tissue in the ventricles to contract in order to optimize the ejection of blood.

1.3 Arrhythmias

Generally human heart rhythm is considered normal if excitation originates in the SA node, is conducted through the normal pathway, and has a regular rate between 60 to 100 beats per minute [12]. But this simple definition, although attractive, cannot account for the complexity of all the cardiac rhythms. According to the standard definition, sinus rhythm less than 60 beats per minute should be regarded as abnormal. But young adults, particularly athletes, frequently display resting heart rates of 40 beats per minute or less, often with intermittent junction escape rhythms and occasionally with AV nodal block [13]. Children and young adults may also manifest irregular heart rates that may be seen as sinus arrhythmia but that, on closer inspection, has no pathological significance. In contrast, these same rhythms in the symptomatic elderly patient are frequently manifestations of serious underlying diseases. A low sinus rate can also suggest an underlying pathology such as hypothyroidism.

The definition of sinus tachycardia is equally imprecise. Although a heart rate of more

than 100 beats per minute is also regarded as abnormal, it may be a normal response to stress. In fact, all cardiac rhythms must be evaluated in the clinical settings in which they are seen. Any evaluation of the significance, untoward effects, and treatment of a disorder of cardiac rhythm is inadequate without the relevant clinical information.

The abnormal rhythm of heart beat is called arrhythmia. This is the most common term and it has become widely accepted, despite the fact that it erroneously suggests an irregularity of the heart beat. On the contrary, many of the arrhythmias have an entirely regular rhythm as, for example, paroxysmal atrial tachycardia, atrial flutter, ventricular tachycardia, complete AV heart block, and others. The term is dysrhythmia. The arrhythmias can be classified among three groups according to their mechanisms: disorders of impulse formation (i.e., those caused by abnormal automaticity), disorders of impulse conduction and disorders produced by abnormalities of both impulse formation and impulse conduction [12].

1.4 Reentry

Tachyarrhythmia is commonly produced by reentry. Reentry is the self-sustained propagation of an activation front in an excitable medium. The onset of reentry requires some form of unidirectional block within a conducting pathway. Furthermore, the effective refractory period of involved action potentials plays a major role in determining whether or not a reentry circuit becomes established [4, 12].

The reentry is the highest probable mechanism of ventricular tachycardias (VT) occurring during the chronic phase of myocardial infarction. It is also the mechanism for atrial flutter. Fig. 1.2 illustrates the requisite conditions for re-excitation by means of a re-entrant circuit. First, a barrier must exist in order to form a circuit. This barrier could be an anatomical or functional obstacle. In the case a ring of tissue, the barrier is the central hole. Second, the conduction time around the ring must exceed the refractory period. In the case of normal cardiac muscle, the long refractory period makes reentry difficult. A locus of abnormally slow conduction may help satisfy the requirement that the transit time exceeds the refractory

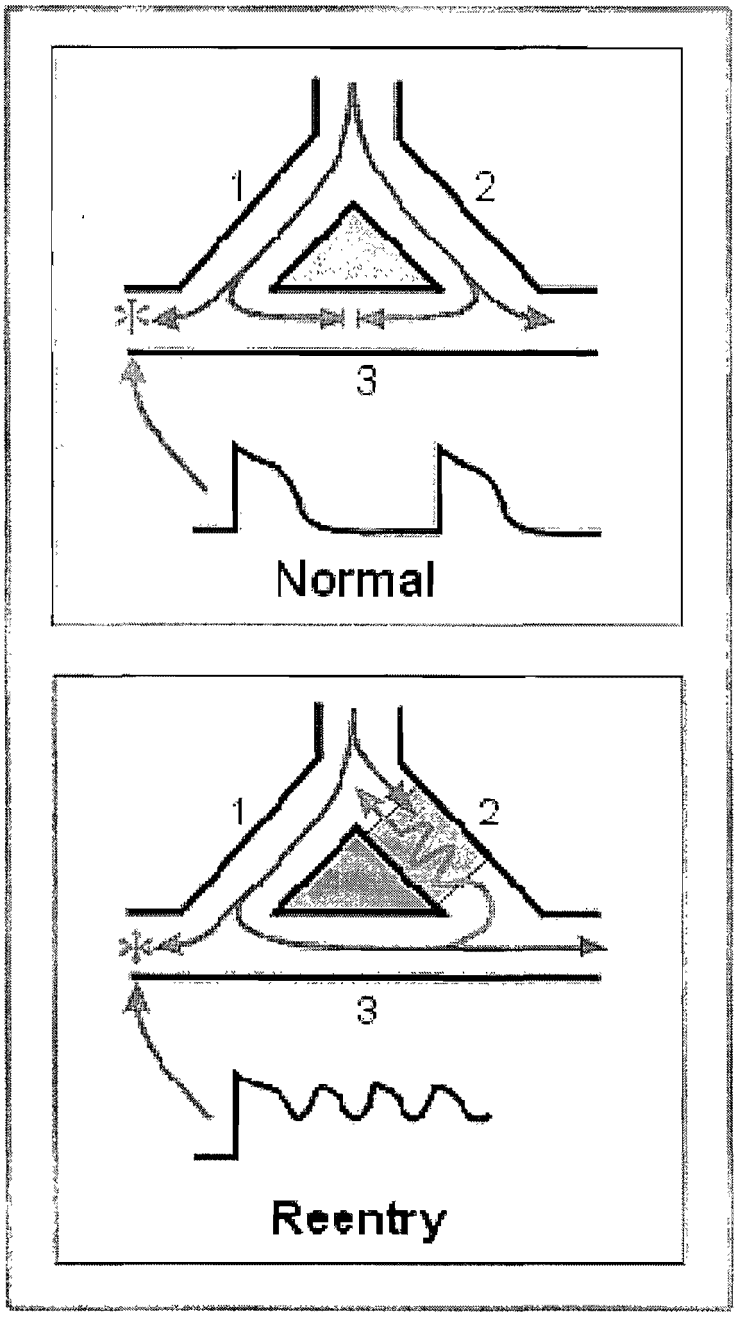

Figure 1.2: Schematic diagram of reentry. Top panel: normal propagation, the excitation propagates through branches 1 and 2, and dies out at position 3. Bottom panel, the branch 2 acts as a site of unidirectional block. When the excitation front comes, the branch 2 is refractory and the excitation only propagates from branches 1 to branch 3. Excitation can then be conducted in branch 2, if it has regained its excitability. If branch 1 is again excitable when the excitation front exits from branch 3, a reentry is established [4].

period of site that is re-excited [4, 12]. In normal propagation, shown in the top panel of Fig. 1.2 the excitation propagates through branches 1 and 2, and dies out at position 3. In the bottom panel of Fig. 1.2, the branch 2 acts as a site of unidirectional block. When the excitation front comes, the branch 2 is refractory and the excitation only propagates from branches 1 to branch 3. Excitation can then be conducted in branch 2, if it has regained its excitability. If branch 1 is again excitable when the excitation front exits from branch 3, a reentry is established.

Even if it represents an oversimplified experimental model of clinical tachyarrhythmias, the study of reentry in rings of cardiac tissue have allowed a careful analysis of a variety of dynamic events that are relevant to ventricular tachycardia occurring around an inexcitable obstacle as well as atrial flutter [8, 14–16]. For a complete understanding of the spatial and time properties of the phenomenon, however, there remain serious complicating factors, such as the anisotropic tissue properties, the spatial disparities in membrane properties and cellular interconnections.

1.5 Beeler-Reuter-Roberge-Drouard Model of the Cardiac ventricular myocyte

1.5.1 Description

Different mathematical models of the electrical properties of ventricular cardiac myocytes have been proposed, they differ in the number of ionic mechanisms that they include [17–20]. In our study, we used the Beeler-Reuter model, as modified by Drouard and Roberge [18,20]. We chose this model because its dynamic properties were thoroughly established both in the space-clamped and continuous one-dimensional ring configurations. Since our goal was to contrast the dynamics in the continuous and discrete one-dimensional loop, we have decided that this was an appropriate choice to analyze the changes specifically induced by discrete intercellular gap junction resistance.

The model includes three voltage and time-dependent Hodgkin-Huxley type currents [19],

the excitatory inward sodium current, i_{Na}, a slow inward calcium current, i_{Ca}, assumed to be carried by calcium ions, and i_{x1}, a K^+ outward current. There is also an additional time-independent outward potassium current, i_{k1}, exhibiting inward-going rectification. The i_{Na} primarily controls the rapid upstroke of the action potential, while the other currents determine the configuration of the plateau and the repolarization phases. In the space-clamped configuration, the variation in membrane potential (V_m, in mV) is expressed by the relation:

$$\frac{dV_m}{dt} = -\frac{1}{C_m}(i_{k1} + i_{x1} + i_{Na} + i_{Ca} - i_{ext}) \tag{1.2}$$

The membrane current density is expressed in $\mu A/cm^2$, while the membrane capacity C_m is set at $1\mu F/cm^2$, the generally accepted value for the capacity of biological membranes C_m [19,20]. i_{ext} corresponds to a stimulus current that can be injected in the internal medium. The scaling of the individual ionic current is chosen to provide current-voltage relationships which match the best estimates obtained experimentally and taken together, produce an acceptable shape for the ventricular action potential. The individual ionic currents (i_{Na}) are given by the relations:

$$i_{Na} = \bar{g}_{Na} m^3 hj(V_m - E_{Na}) \tag{1.3}$$

where $\bar{g}_{Na} = 15mS/cm^2$ is the maximum conductance of the sodium ($mS/cm^2 = 1/K\Omega/cm^2$) and where E_{Na} is the Nernst potential associated to the Na^+ ions (fixed at $-40mV$). The state of each sodium channel is controlled by three types of independent gates that can be open or close: one activation gates (m), and two inactivation gates (h and j). The variables m, h, and j represent the proportions of each type of gates that are in the open state.

The individual ionic currents (i_{Ca}) are given by the relations:

$$i_{Ca} = \bar{g}_{Ca} df(V_m - E_{Ca}), \tag{1.4}$$

where $\bar{g}_{Ca} = 0.09mS/cm^2$ is the maximum conductance of the calcium, the d and f are the proportion of the activation gates and inactivation gates of the Ca^{2+} channels in the open

state, respectively. E_{Ca}, the calcium Nernst potential, varies with the internal concentration of $[Ca]$ (mM) according to the relation:

$$E_{Ca} = -82.3 - 13.0287ln[Ca] \tag{1.5}$$

The dynamics of $[Ca]$ is described by the relation:

$$\frac{d[Ca]}{dt} = -10^{-7}i_{Ca} + 0.07(10^{-7} - [Ca]) \tag{1.6}$$

The time dependent activated outward potassium current i_{x1} is given by

$$i_{x1} = \bar{i}_{x1}x_1. \tag{1.7}$$

where x_1 is the activation gate variable and $\bar{i}_{x1}$ is given by

$$\bar{i}_{x1} = \frac{0.8\{exp[0.04(V_m + 77)] - 1\}}{exp[0.04(V_m + 35)]}. \tag{1.8}$$

The time-independent potassium current exhibiting inward-going rectification (i_{k1}) is given by

$$i_{k1} = 0.035\{\frac{4(exp[0.04(V_m + 85)] - 1)}{exp[0.08(V_m + 53)] + exp[0.04(V_m + 53)]} + \frac{0.2(V_m + 23)}{1 - exp[-0.04(V_m + 23)]}\}, \tag{1.9}$$

the dynamics of the gate variable m, h, j, d, f and $x1$ is described by the relation

$$\frac{dy}{dt} = \alpha_i(1 - y) - \beta_i y \tag{1.10}$$

$$\frac{dy}{dt} = (y_\infty - y)\tau_i, \tag{1.11}$$

where y_∞ and τ_i are related to the rate constants of the transition from close to open state (α) and open to close state (β) by the relation

$$y_\infty = \frac{\alpha_i}{\alpha_i + \beta_i} \tag{1.12}$$

$$\tau_i = \frac{1}{\alpha_i + \beta_i} \tag{1.13}$$

The voltage-dependent rate constants α and β are given by

$$\alpha(\beta) = \frac{C_1 exp[C_2(V_m + C_3)] + C_4(V_m + C_5)}{exp[C_6(V_m + C_3)] + C_7} \tag{1.14}$$

Table 1.1: C, defining function and values for rate constants (α and β)

Rate constant	$C_1\ ms^{-1}$	$C_2\ mV^{-1}$	$C_3\ mV$	$C_4\ (mVms)^{-1}$	$C_5\ mV$	$C_6\ mV^{-1}$	C_7
α_m	0	0	42.65	-0.818	42.65	-0.22	-1
β_m	1.437	-0.085	39.75	0	0	0	0.1
α_h	0.1	-0.193	79.65	0	0	0	-0.4
β_h	2.8	0	20.5	0	0	-0.095	1
α_j	0.055	-0.25	78	0	0	-0.2	1
β_l	0.3	0	32	0	0	-0.1	1
α_d	0.095	-0.01	-5	0	0	-0.072	1
β_d	0.07	-0.017	44	0	0	0.05	1
α_f	0.012	-0.008	28	0	0	0.15	1
β_f	0.0065	-0.02	30	0	0	-0.2	1
α_{x1}	0.0005	0.083	50	0	0	0.057	1
β_{x1}	0.0013	-0.06	20	0	0	-0.04	1

the constants $C_1, C_2, C_3, C_4, C_5, C_6$, and C_7 are given by table 1.1. The dynamics of these gates variables follow the formulation first proposed by Hodgkin and Huxley [19]. Using this approach, with a fixed membrane potential V_m, the proportion of any specific gate populations in the open state converges toward a voltage dependant steady-state $y_{i,\infty}(V_m)$ with a characteristic time constant $\tau_i(V_m)$. If $y_{i,\infty}(V_m)$ is small at low V_m values and increased toward 1 as V_m is increased, the y_i gate is said to be an activation variable, and is called an inactivation variable in the inverse case. Typically, the value of the steady-state and time constant function of the gate variable are obtained by fitting the experimental results obtained using the voltage-clamp technique [19]. In essence, this technique involves abruptly changing the transmembrane potential from an initial value to a predetermined clamp potential and maintaining this clamp potential constant by the injection of a feedback current despite changes in the membrane conductance. It involves different procedures in order to isolate the contribution of a specific current, as well as multistep protocols to obtain characteristics of the activation and inactivation gates when they contributed together to the dynamics of the current [21, 22].

1.5.2 Dynamics on the Space-Clamped MBR

The Figure 1.1 shows the action potential obtained from the MBR model stimulated from rest by a square current pulse of 1 ms. The dynamics of the space-clamped MBR model have been studied both for the presence of constant bias currents and repetitive pacing with square pulses of current. In the case of the constant bias current, it was shown that there was an interval over which the model is automatic, producing repetitive action potentials [23]. However, the results obtained with pacing are more relevant to the present work on reentry.

For pulse stimulation, the response of the MBR model is all or none [24]. If the current is below a threshold, it produces a small passive depolarization and repolarizes as soon as the stimulus is removed. If the stimulus is above the threshold, it produces an action potential as in Fig. 1.1, whose duration does not depends on the intensity of the stimulus above the threshold. This can be seen in the Fig. 1.3, which shows the stable entrainment response of the model to 40 $\mu A/cm^2$ square pulses of current of $1ms$ duration applied at two different basic cycle lengths (BCL = 1000 and $350ms$). In both cases, the system produces a stable period-1 repetitive response with fixed action potential duration (A) and diastolic interval (D) that it reaches after a transient period at the beginning of pacing. During the plateau of the action potential, the slow inactivation variable f controlling i_{ca} closes, and the slow activation variable x_1 of i_k opens, both contributing to the repolarization. Then, these gates variables return toward their respective resting value during the next diastolic interval. However, as BCL is decreased, they do not have the time to recover completely, leading to a buildup of the x_1 and a gradual decrease f, which lead together to an abbreviation of the action potential duration. Period-1 response corresponds to an equilibrium, where x_1 and f reach a mean value such that the changes occurring during the depolarized phase are exactly compensated by the recovery during the next diastolic interval.

The value of the threshold current (I_{thr}) depends on the duration of the pulse, and on the prematurity of the stimulation. The action potential duration is also a function of prematurity. As shown in Fig. 1.4, the prematurity can be measured by the time interval

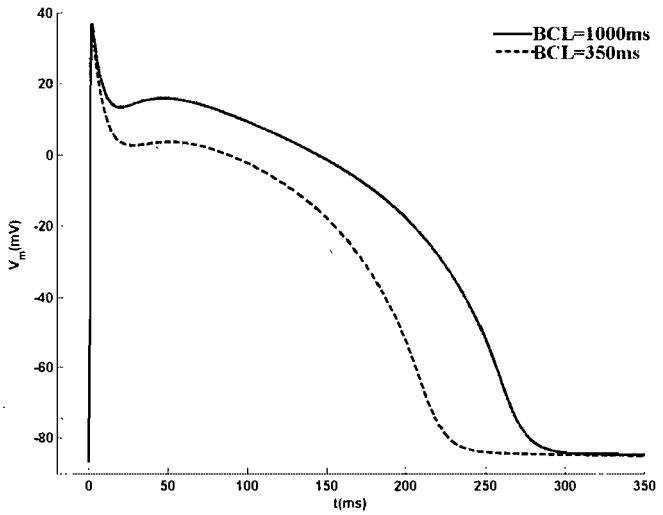

Figure 1.3: The action potential duration is also a function of prematurity, This graph shows the stable entrainment response of the model to 40 muA/cm^2ms square pulses of current of 1 ms duration applied at two different basic cycle lengths (BCL = 1000 and 350ms). The duration of the action potential is reduced when the BCL, which is the time between the successive stimuli, becomes shorter [23].

between the onset of the new stimulus $S2$ and that of the previous stimulus $S1$ having produced an action potential, the so-called $S2 - S1$ interval. Alternately, prematurity can also be measured by the diastolic interval D, consisting of in the time span between the end of the previous action potential and the onset of the new stimulus $S2$. For the MBR model, the action potential duration (A) is defined to end at the moment when V_m reaches -50 mV in repolarization. The restitution curve, giving the duration of the action potential as a function of the prematurity of the stimulus, provides a global picture of variation in the action potential duration. As illustrated in Fig. 1.5, the restitution curve can be constructed by first obtaining stable entrainment of the system for a given BCL pacing, and then applying $S2$ stimuli with a varying prematurity on the reference action potential. The duration of the resulting action potential for each value of the $S2 - S1$ interval are recorded.

Fig. 1.5 shows the restitution curves obtained after a pacing of BCL at 1000 and 350ms, of which stable responses are displayed in Fig. 1.4. The two restitution curves are different because the action potentials after which S2 is applied are different. The action potential

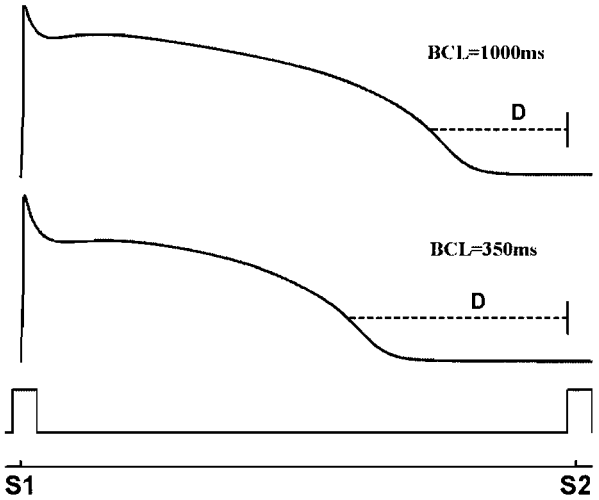

Figure 1.4: The two different basic cycle lengths ($BCL = 1000$ and $350ms$). Two stimuli $S1$ and $S2$ applied [23].

duration of the stable entrainment response at $BCL = 350ms$ is much shorter than the action potential obtained at $BCL = 1000ms$. In consequence, the absolute refractory period at $BCL = 1000ms$ is longer, as the minimal $S2 - S1$ interval to obtain an active response is longer. The two restitution curves expressed as a function of $S2 - S1$ appear to be shifted, relative to each other. However, as seen in the right panel of Fig. 1.5, the two curves are almost identical when A is expressed as a function of the diastolic interval ($[S2 - S1] - A_s$, the A_s of the response to pacing). In reference [23], it was shown that the $A(D)$ restitution curves of the MBR model were almost identical for reference action potentials obtained from a wide range of pacing frequencies and durations of square pulse stimulation. It was also shown that $I_{thr}(D; T_{pulse})$, the variation of threshold current as a function of the diastolic interval for each duration T_{pulse} of the square pulse stimulus, was also an invariant function for each duration. Memory effect, by which the threshold and/or the A would depend not only on the last action potential but also on the preceding sequence of activations, can therefore be neglected in the standard MBR model. However, it was shown that for some modifications of the MBR model, such as shortening the time constant of i_{Ca} gate variables,

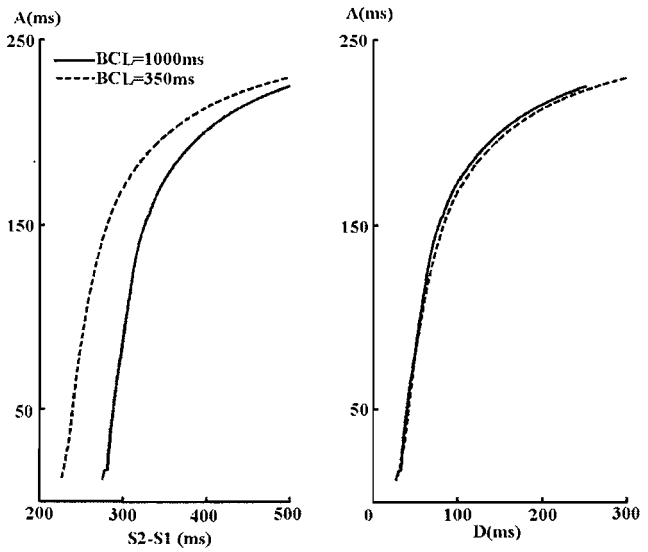

Figure 1.5: Action potential duration (A) obtained by premature stimulations of the stable response at two BCL. $S2 - S1$ is the time from onset of the last pacing stimulus to the premature stimulation. D is the time from the end of the action potential to the onset of the premature stimulation. Left panel: A changes when expressed as a function $S2 - S1$. Rigth Pannel: When A is expressed as a function of D, the two curves merge, showing that A only depends on D [23].

the memory effect could no longer be neglected [25, 26].

As it will be explained below, the invariance of the A and I_{thr} curve as a function of D permits understanding of the change in entrainment response with respect to the frequency of stimulation. Fig. 1.6 shows the stable entrainment response of the model to $40\mu A/cm^2$ square pulses of current of $1ms$ duration applied at different BCL. In each of the two top panels, all stimuli produced the same action potential. This entrainment can be called a 1:1 response, meaning that each stimulus produces the same active response. However, as expected, the duration of the action potential is reduced when the BCL is shortened. The two subsequent panels, with $BCL = 265$ and 260 ms, show another type of entrainment where each stimulus still produces an active response, but with duration alternating between a long and short action potential. This can be called a 2:2 entrainment, meaning that the periodic pattern of response repeats after two stimuli and induces two different active responses. Finally, at a shorter BCL in the bottom panel, the pattern of response still repeats

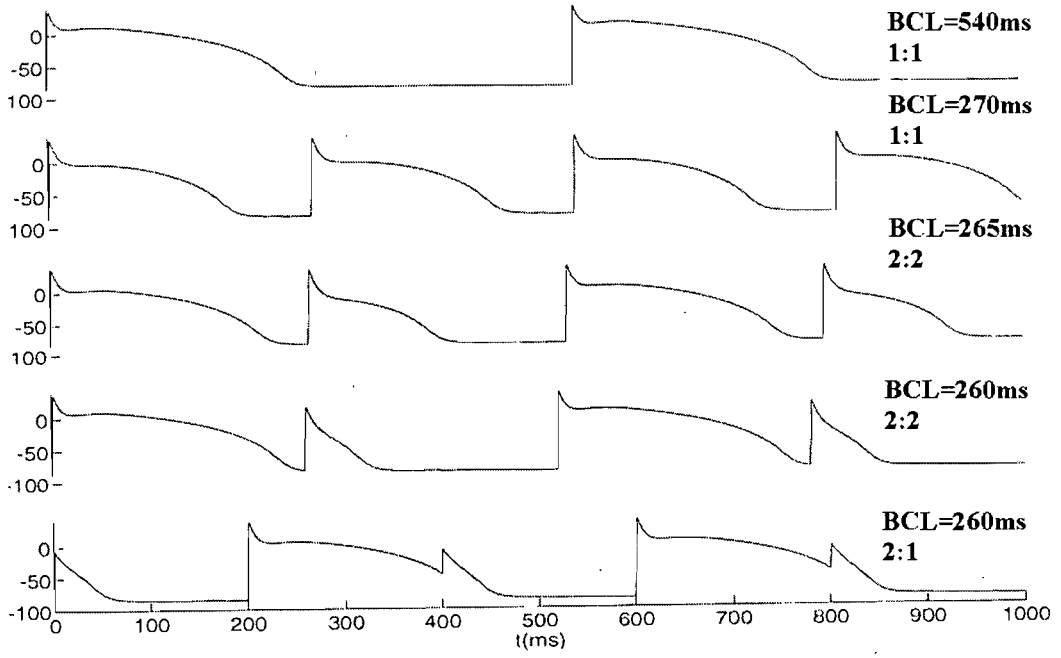

Figure 1.6: The first and the second rows show 1:1 response, the third and the forth rows show 2:2 response and the last row shows 2:1 response.

after two stimuli but each periodic sequence contains an active and a passive response, a rhythm that can be called a 2:1 response. Fig. 1.7, showing the maximum inward current following each stimulus, provides a synthetic view of the bifurcations.

Fig. 1.8 provides a schematic representation of the dynamics for producing successive stimuli that provoke an active response during pacing at a fixed BCL. D_i, the diastolic interval preceding the onset of the ith stimulus, is equal to $BCL - A_{i-1}$, where A_{i-1} is the duration of the action potential produced by the stimulus $i-1$. Since A is only a function of the diastolic interval, this relationship leads to the finite-difference (FD) equation:

$$D_i = BCL - A(D_{i-1}) \tag{1.15}$$

A 1:1 response corresponds to a fixed point (i.e. $D_i = D_{i+1} = D_s$) of the system and is stable if and only if

$$|\frac{dA}{dD}|_{D_s} < 1 \tag{1.16}$$

The finite-difference FD model, based on the invariance of the $A(D)$ function predicted

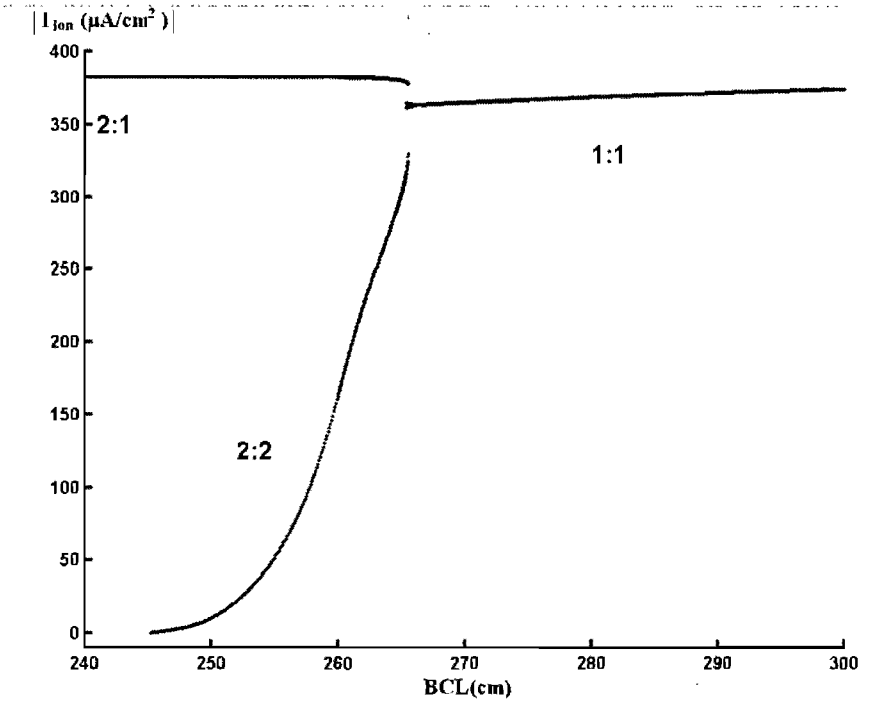

Figure 1.7: The maximum inward current ($|I_{ion}(\mu A/cm^2)|$) following each stimulus provides a synthetic view of the bifurcations.

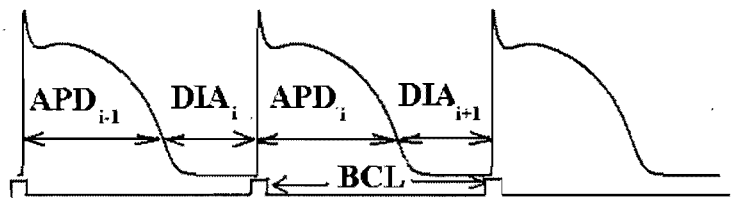

Figure 1.8: The Schematic diagram gives the relationship between BCL, APD and DIA.

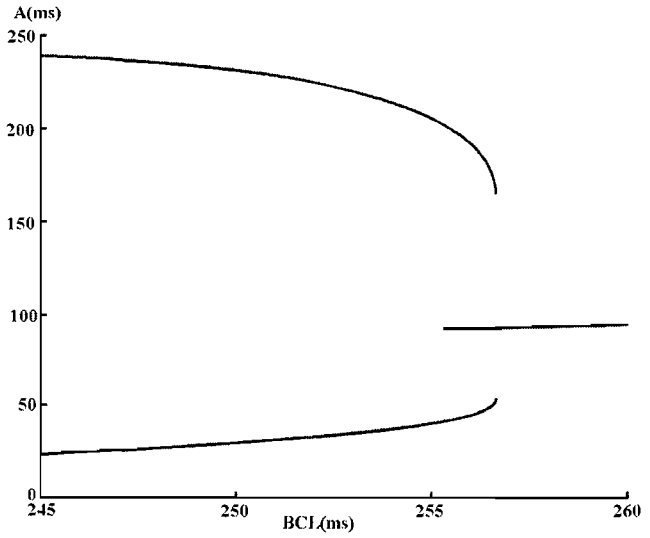

Figure 1.9: The finite difference model reproduces the bifurcation of the MBR model. The model was simulated using $A(D)$ function fitted from Fig. 1.7.

that the 1:1 response loses its stability when A and D fall on the portion of the restitution curve where the slopes are greater than 1. Fig. 1.9 presents the bifurcation from 1:1 to 2:2 predicted by the FD model, with $A(D)$ fitted from Fig. 1.7. It reproduces the nature and the position of the bifurcation obtained in the MBR model. In fact, the FD model, complemented by rule to account for the threshold and the absolute refractory period, has also been shown to correctly reproduce the complex bifurcation structure, appearing with respect to the BCL and the amplitude of stimulation. However, as we shall see in the next section, the bifurcation from 1:1 to 2:2 response is the most relevant with respect to reentry.

1.6 Modified Beeler-Reuter Loop Model

The bifurcation from 1:1 to 2:2 response observed as the frequency of pacing is increased in the space-clamped MBR model suggests that transitions may also occur during reentry. Much work has been done on reentry in a one-dimensional loop, using either ionic models or low-dimensional representations of the dynamics [25, 27–36]. Most of the studies using ionic models have used the cable equation, which considers the membrane as an homogeneous

and continuous cylinder, the extracellular medium as an equipotential and neglects the radial current in the intracellular medium [21]. With these hypotheses, the evolution of the membrane potential V on a loop of length L is described by the partial differential equation:

$$\frac{1}{\rho}\frac{\partial^2 V^i(x,t)}{\partial x^2} = S[C_m\frac{\partial V^i(x,t)}{\partial t} + I^i_{ion}(x,t)], \quad x\epsilon[0,L] \tag{1.17}$$

with the boundary condition

$$V(0,t) = V(L,t) \tag{1.18}$$

where ρ $(K\Omega{\cdot}cm)$ is the constant axial intracellular resistivity, C_m $(\mu F/cm^2)$ is the membrane capacitance and S $(1/cm)$ is the ratio of the surface of the membrane to the volume of the intracellular medium. $I_{ion}(x,t)$ is the ionic current crossing the membrane. For the MBR model presented in the previous section, the dynamics variables $(y_i, i = 1,6)$ and $[Ca_i]$ become functions of space and time in such a way that their equations must be solved at each site of the membrane. There is no diffusive term for these variables, but they must fulfill the boundary conditions $(y_i(0,t) = y_i(L,t)$, $[Ca_i(0,t)] = [Ca_i(L,t)]$. Diverse numerical methods exist for solving this type of system [27,34]. We present here a numerical method devised for parallel processing [27]. This method is described in Appendix I of this thesis, we have modified for the loop with discrete gap junction resistances. The loop is first divided in a number of segments $(j = 1, N)$ of length L_c and the system is solved with a constant time step Δt. For each time step, the system describes the spatial evolution of V within each segment at time $t + \Delta t$ becomes an ordinary differential equation:

$$\frac{d^2 Vj(x,t+\Delta t)}{dx^2} = \frac{\rho SC_m}{\Delta t}V^j(x,t+\Delta t) - \frac{\rho SC_m}{\Delta t}V^j(x,t) + \rho SI^j_{ion}(x,t) \tag{1.19}$$

Since all the quantities at time t are known, this system is equivalent to:

$$\frac{d^2 Vj(x)}{dx^2} - K^2 V^j = g^j(x) \;\; x\epsilon[0,L_c] \;\; j = 1\ldots N \tag{1.20}$$

With the boundary conditions:

$$V^j(0) \;\; = \;\; V^{j-1}(L_c), \quad j = 2, N-1 \tag{1.21}$$

$$V^1(0) = V^N(L_c), \tag{1.22}$$

$$\frac{dV^j(0)}{dx} = \frac{dV^{j-1}(L_c)}{dx} \quad j = 2, N-1 \tag{1.23}$$

$$\frac{dV^1(0)}{dx} = \frac{dV^N(L_c)}{dx} \tag{1.24}$$

These conditions assure the continuity of the voltage and of the axial current between the segments of the loop.

The solution of Eq.(1.20) is given by the sum of a particular solution V_p^j and of the solution V_H^j of the homogeneous system;

$$V_H^j = A_j e^{Kx} + B_j e^{-Kx} \tag{1.25}$$

The V_p^j is obtained by solving Eq.(1.20) for each segment with the Neumann boundary conditions:

$$\frac{dV_H^j(x)}{dx}|_{x=0,L_c} = 0 \tag{1.26}$$

To obtain this particular solution, each segment is discretized with a constant spatial step of Δx and the system is solved by using a linear finite element method [34]. Then the segments are reconnected by calculating the A_j and B_j to fulfill the continuity conditions. Reentry can be initiated by disconnecting the loop, stimulating one of the free ends and then closing the loop after a delay. Once reentry has stabilized, it is possible to shorten the loop gradually to investigate the effect of the circumference on the dynamics of reentry. Quan and Rudy [35] have shown that reducing the loop length results in an increased degree of head-tail interaction that, in turn, brings about shortening and eventually alternation in action potential durations. Vinet et al. [27,28] as well as Courtemanche et al [30,31], working respectively with the MBR model and the original BR model, have provided a complete study of the effect of the loop length.

Results for the MBR model are presented in Fig. 1.10 (A). For each loop of length L, measurements are taken at one site for multiple turns. For a long L, the cycle length, which is the time between successive action potentials at the site of measuring, is constant. Moreover, the action potential duration (APD: from the time of the upstroke to $-50mV$

downcrossing in repolarisation), the diastolic interval (DIA: from the end of the action potential to the next upstroke) are the same for all successive action potentials. In this case, the reentry is periodic (period-1) and corresponds to a fixed waveform traveling at constant speed around the loop. As the loop is shortened, the cycle length decreases because the speed of propagation remains almost constant. Both DIA and APD also diminish, they take place in a space-clamped membrane when the pacing frequency is increased. Then, below a critical length X_{crit}, the cycle length, DIA and APD become multiple values. At X_{crit}, the cycle length has exactly the value for which there is a transition from 1:1 to 2:2 response in the space-clamped model. However, the response is not 2:2 in the loop but rather wanders between an upper and a lower bound. These bounds part as L becomes shorter, until a minimum X_{min} below which sustained reentry becomes impossible.

To get a clear picture of reentry below X_{crit}, propagation must be followed as it proceeds along the loop, recording successive APD and DIA values at each site. Fig 1.11 shows the spatial variation of DIA along the loop for successive turns abutted end-to-end. There is a spatial oscillation of DIA as propagation proceeds, with a wavelength that is an irrational fraction of L. Hence, the sequence of DIA measured at one site becomes quasiperiodic (QP). As shown in figure 1.11, two different types of QP reentry were observed on the MBR loop, one with a wavelength close to $2L$, and a second with a wavelength close to $2/3L$.

Courtemanche et al. [31] have extended the FD model that was developed for the paced space-clampe. As for the FD model, APD is assumed to be a function of the previous action potential, which yields

$$DIA_i(x) = CL_i(x) - APD(DIA_{i-1}) \tag{1.27}$$

where $DIA_i(x)$ stands for the diastolic interval of the ith action potential at site x, and $CL_i(x)$ is the cycle length between the new activation and the previous one. If the successive turns are abutted end-to-end and x is extended to span multiple loop length L, $DIA_{i-1}(x)$ would be the value that occurred at position $x - L$. The equation can be rewritten as a

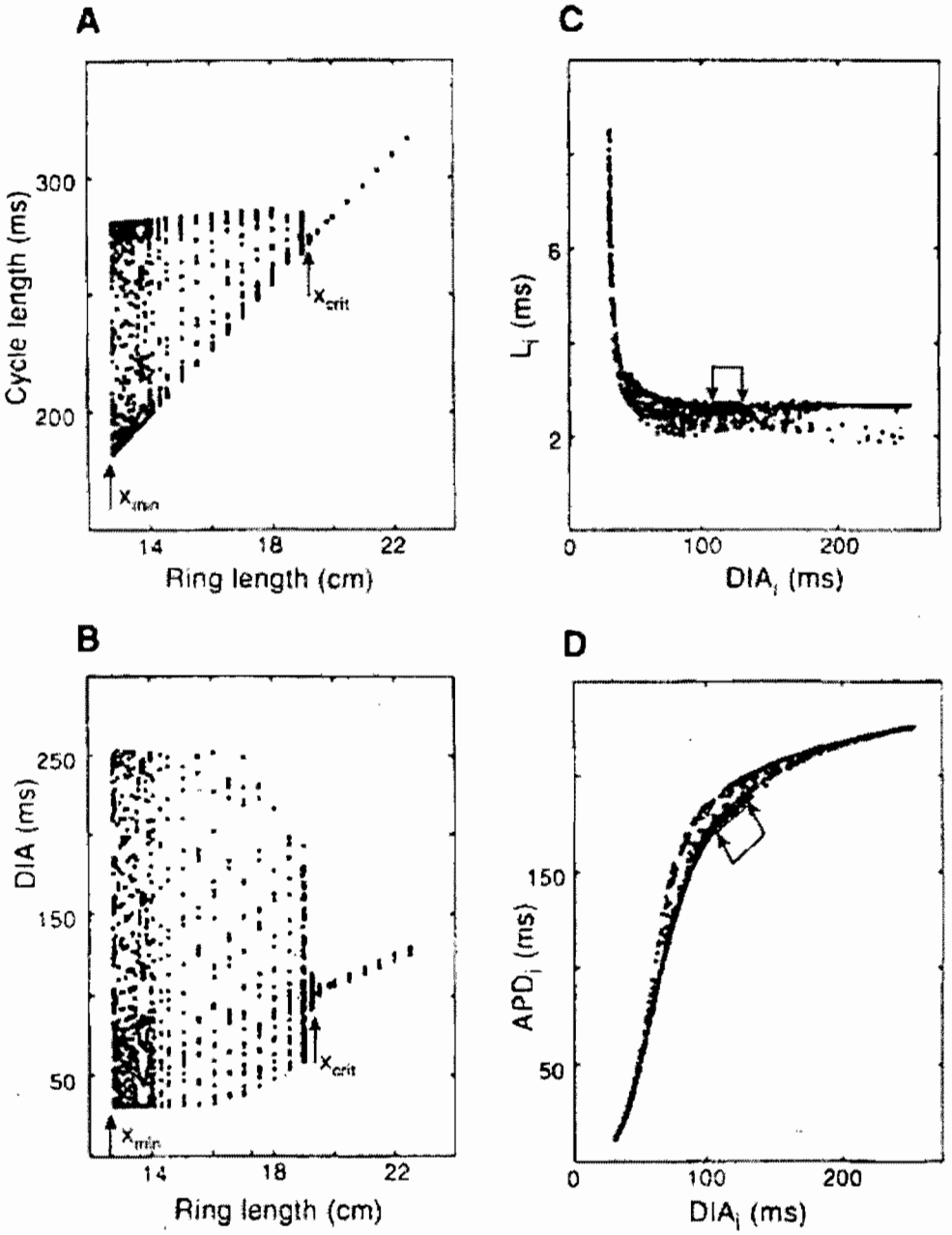

Figure 1.10: Analysis of temporal activity recorded at a single point on rings of different lengths. (A and B) CL and DIA for a maximum of 25 successive turns at each ring length. Stable reentry occurs for $X > X_{crit} = 19.6cm$, complete block for $X < X_{min} = 12.8cm$, and irregular propagation for $12.8cm < X < 19.6cm$. (C and D) Scatter diagrams of latency and APD versus DIA for all patterns displayed in (A) and (B). Arrows in (C) and (D) indicate the set of points corresponding to stable reentry ($X > 19.6cm$) [27].

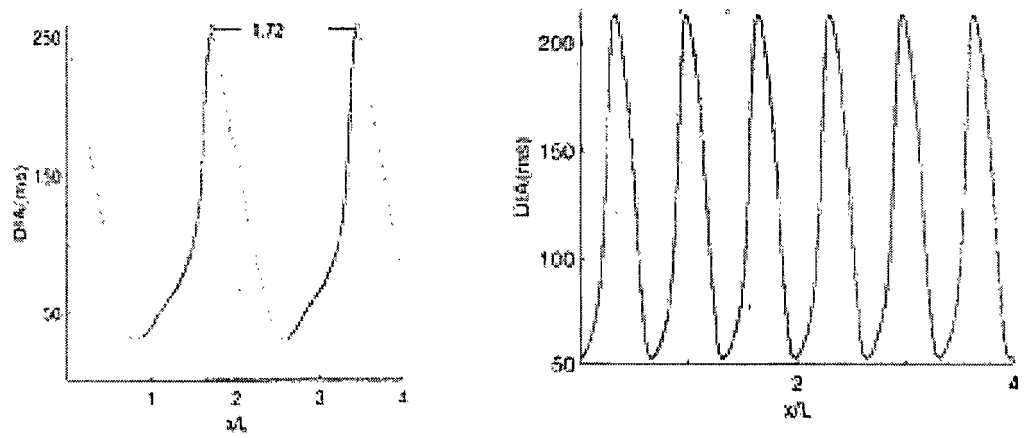

Figure 1.11: Mode-0 at $L = X_{min} = 12.8$cm, and mode-1 at $L = 18.65$cm, MBR model [29].

delay equation:

$$DIA(x) = CL(x) - APD(DIA(x - L)) \tag{1.28}$$

The last hypothesis, appropriate for the BR and MBR models, is that the speed of propagation θ is also a function of DIA. Then,

$$CL(x) = \int_{x-L}^{x} \frac{1}{\theta(DIA(y))} dy \tag{1.29}$$

and the complete model becomes an integral-delay equation:

$$DIA(x) = \int_{x-L}^{x} \frac{1}{\theta(DIA(y))} dy - APD(DIA(x - L)) \tag{1.30}$$

Courtemance et al. [31] have analyzed the stability of the constant solution ($DIA(x) = constant$) corresponding to period-1 reentry. They have proven that it remains stable until $DIA = DIA_{crit}$ where

$$\left| \frac{d(APD)}{d(DIA)} \right|_{DIA_{crit}} = 1 \tag{1.31}$$

Hence, the criterion for the stability of the 1:1 response in the paced space-clamped model also controls the stability of the period-1 reentry in the loop. Furthermore, they have also proven that an infinite number of quasiperiodic mode of reentry appears at the bifurcation, with wavelength

$$\lambda_n \approx \frac{2L}{2n+1}, \quad n \epsilon [0, \infty] \tag{1.32}$$

The two modes of reentry shown in Fig. 1.11 have a wavelength close to $n = 0$ and $n = 1$ respectively, and are accordingly designated as mode-0 and mode-1 reentry. These two modes were observed in the BR and MBR models. In both cases, mode-0 reentry was shown to appear through a supercritical Hoph bifurcation. The amplitude of the spatial DIA oscillation grows from 0 as L is shortened below X_{crit}, and reaches a maximum at X_{min}, where sustained reentry stops. Vinet et al. [27] found that the mode-1 reentry to display a large amplitude at a length shorter than X_{crit} and to disappear when L is larger than X_{min}. Higher modes ($n > 1$) of propagation were never observed, even after a systematic search for appropriate initial conditions [27, 29]. Although successful in predicting the loss of period-1 solution, the integral-delay model could not explain the difference in the way mode-0 and mode-1 are created, as well, the absence of $n > 1$ modes goes unexplained. Vinet et al. also observed that the APD vs DIA relationship was becoming dual value (Fig. 1.10(D)) in quasiperiodic reentry. They suggested that this was a consequence of the effect of coupling on repolarization, by which the surrounding of a point influences its repolarization and modifies the APD [29,37,38]. They proposed to include in the integral-delay model the effect of coupling on APD through the equation:

$$APD(x) = \int_{-u}^{u} w(y) APD_r(DIA(x+y))dy \tag{1.33}$$

where $APD_r(DIA)$ is the restitution curve as in the DF model, $w(y)$ is a weighting function chosen as a normalized Gaussian (i.e. $w(0) = 1$), and u is the extent of the neighborhood influence. This led to the modified integral delay model

$$DIA(x) = \int_{x-L}^{x} \frac{1}{\theta(DIA(y))}dy - \int_{-u}^{u} w(y) APD_r(DIA(x-L+y))dy \tag{1.34}$$

As shown in Fig. 1.12, the modified integral-delay model can correctly reproduce the bifurcation structure of the MBR model as well as the multiple-value APD vs L relationship observed in quasiperiodic propagation. Formal analysis of the model [29, 37, 38] also shows that the coupling displaces the value of the loop length at which the mode is created and may forbid the appearance of higher modes. The study of bifurcation has been extended to

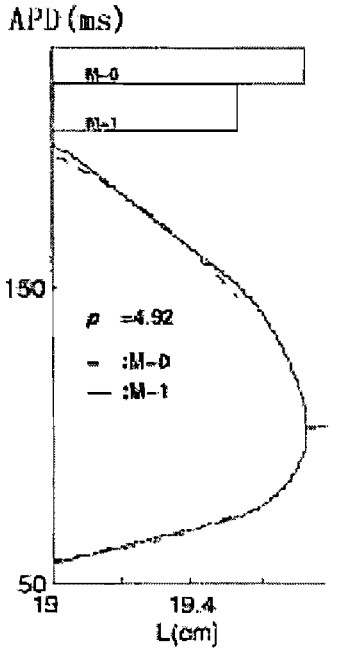

Figure 1.12: Mode-0 is represented by the solid line, and mode-1 is given by the dash line as a function of L [29].

the two-dimensional ring, a more complex system due to additional contribution of curvature of activation and repolarization front to the stability of reentry [39–42].

1.7 Role of gap junction in the propagation of the cardiac action potential

Real cardiac tissue does not form a syncytium as hypothesized in the cable equation. Rather, the tissue is formed by discrete myocytes electrically connected by gap junction resistances such the cell to cell propagation is discontinuous [43, 44]. Gap junctions play an important role in the velocity and the safety of impulse propagation in cardiac tissue. Under physiologic conditions, the specific subcellular distribution of gap junctions together with the tight packaging of the rod-shaped cardiomyocytes underlies anisotropic conduction, which is continuous at the macroscopic scale. During gap junction uncoupling, discontinuities reappear and are accompanied by slowed and meandering conduction. Junction resistance can be modulated to obtain very high values in abnormal cases such as ischemia and infarction,

Figure 1.13: Gap junction in the series branches of myocytes from the most superficial layer of the monkey's right ventricle (1660×). They consist of steps and risers [45].

leading to very slow conduction. In extreme cases, it may lead to complete decoupling of neighboring cells, resulting in a conduction block. Fig. 1.13 shows an electron microscope picture of the gap junctions in myocytes extracted from a monkey's right ventricle.

The cellular structure of the myocardium is important for understanding both normal propagation and arrhythmogenesis. Structural anisotropy may be related to cell shape and also to the cellular distribution pattern of proteins involved in impulse conduction, such as gap junction connexins and membrane ion channels. The functional connections between cardiac cells, consisting of so-called gap junctions, vary in their molecular composition, degree of expression and distribution pattern. Each of these variations may contribute to the specific propagation properties of a given tissue in a given species. The gap junction is formed by the junction of two connexin proteins, each being embedded in the membrane of one cell. Fig. 1.13 presents a schematic representation of a gap junction connexin protein. There exist different forms of connexin as Fig. 1.14 demonstrate [46–50]. Connexin 43 (Cx43) is the most abundant protein in the heart and is also present in many other organs. Cx43 can

be found in the ventricle, atria and the ventricular conducting system [46, 51–55] while its presence is disputed in the sinoatrial node and in the atrioventricular node [46,53,54,56–58]. $Cx40$ plays an important role in the atria, the atrioventricular node, and the ventricular conducting system [46, 51, 53, 59–62]. Due to its large single-channel conductance, $Cx40$ is likely to contribute to a high propagation velocity in parts of the atria (crista terminalis) and the specific ventricular conducting system. While some studies have shown expression of $Cx45$ in most myocytes [60], its role in impulse conduction in the ventricle is not fully clarified. A further, still not fully answered question relates to the functional consequences of colocalization of different connexins in gap junctions. Such colocalization may reflect heterotypic or heteromeric gap junctions with electric properties that are different from the properties of corresponding homotypic or homomeric channels shown as Fig. 1.14. While such formation has shown to produce a multitude of electric conductance states in vitro [63–67], their functional role in vivo still remains to be defined [68].

Fig. 1.15 presents a simple model of a one-dimensional strand of cardiac cells joined by gap resistances. In this model, all the gap junction channels are lumped in a single value of resistance which is assumed to be constant.

Keener has published a theoretical analysis on the space-constant of a passive discrete one-dimensional cable [69]. In his approach, each cell is considered a continuous cable of length L, internal section A_i, circumference p, axial resistivity ρ_i and capacitance C_m. It is surrounded by a continuous external medium of section A_e and resistivity ρ_e. The evolution of the intracellular and extracellular potentials V_i and V_e within each cell are given by the equations:

$$\frac{A_i}{\rho_i}\frac{\partial^2 V_i}{\partial x^2} = p(C_m\frac{dV}{dt} + I_{ion}) \tag{1.35}$$

$$\frac{A_e}{\rho_e}\frac{\partial^2 V_e}{\partial x^2} = -p(C_m\frac{dV}{dt} + I_{ion}) \tag{1.36}$$

where $V = V_i - V_e$ is the membrane potential. The intracellular medium of the cells are connected by a gap junction of resistance r_g, while the external medium is continuous. If the width of the gap junction is neglected, the connection between the n_i^+th and $n + 1_i^-$th

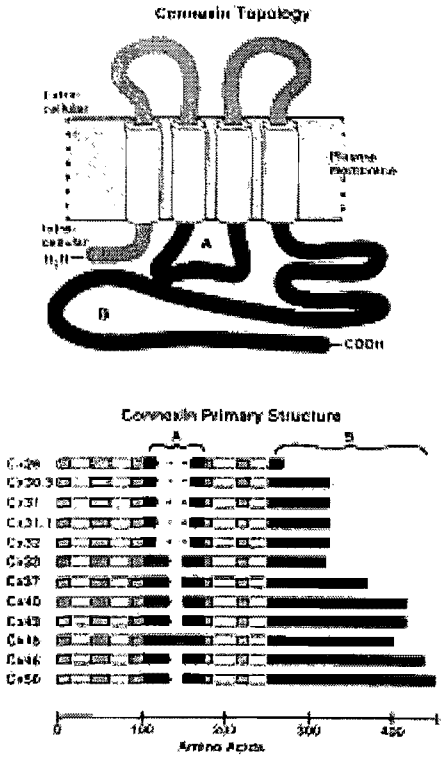

Figure 1.14: Top panel: the molecule of connexion topology, the transmembrane is shown as white, the N-terminal is shown as grey, the tail C-terminal are black. The bottom panel, the sequences of amino acids of the different connexion, starts from N-terminal [50].

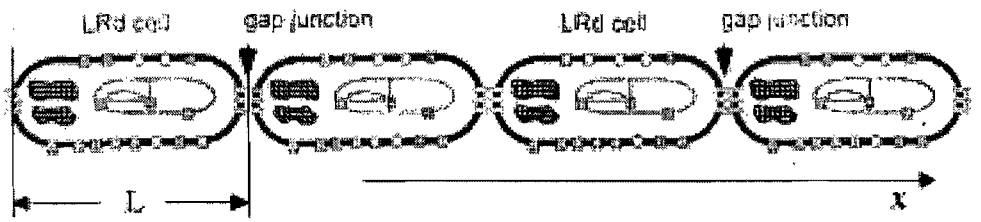

Figure 1.15: A small segment of the theoretical model with the gap junction [70].

cell is equivalent to the continuity condition, this condition states that the axial current is continuous between the cells. When the current flows in the gap junction resistance, it causes a difference of potential between the end of a cell and the beginning of the following cell.

If V_e is assumed to be an equipotential as in Eq.(1.35), the system can be rewritten as

$$\frac{1}{\rho_i}\frac{\partial^2 V}{\partial x^2} = \frac{p}{A_i}(C_m\frac{dV}{dt} + I_{ion}) = S(C_m\frac{dV}{dt} + I_{ion}) \tag{1.37}$$

This is the cable equation applied within each cell, with boundary condition:

$$\frac{A_i}{\rho_i}\frac{\partial V(x = nL^-)}{\partial x} = \frac{A_i}{\rho_i}\frac{\partial V(x = nL^+)}{\partial x} = \frac{V(nL^+) - V(nL^-)}{r_g} \tag{1.38}$$

This is the formalism that we have adopted to study the dynamics of the discrete one-dimensional loop that is presented in the following chapter.

The goal of Keener was to obtain an expression for the space-constant of the system Eq.(1.35) assuming a passive membrane current given by:

$$I_{ion} = \frac{V}{R_m} \tag{1.39}$$

where R_m is the resting membrane resistance. He has obtained an analytical expression for the asymptotic profile of V_i and V_e (i.e. $\frac{\partial V_{i,e}}{\partial t} = 0$) on a finite cable ($x = [0, L]$) with a constant current injected at $x = 0$ and no flux boundary condition at the other end. Fig. 1.16 shows an example of the resulting asymptotic profile of V_i and V_e [69]. There is a smooth decrease of V_e because the extracellular medium is continuous. V_i has a saw-tooth appearance due to the gap junction resistance.

Rudy, working with different collaborators, has published a series of articles on the influence of discrete gap junction coupling in a linear strand model of cardiac cells, using either the BR model [73] or the so-called Luo-Rudy II model [70, 74]. As shown in figure 1.17 (velocity θ) [73] and figure 1.18 (time delay) [73], the velocity in a cell increases with increasing disk resistance, reflecting the fact that the current is more confined to the cell, therefore, more current is available to depolarize the cellular membrane. On the other hand,

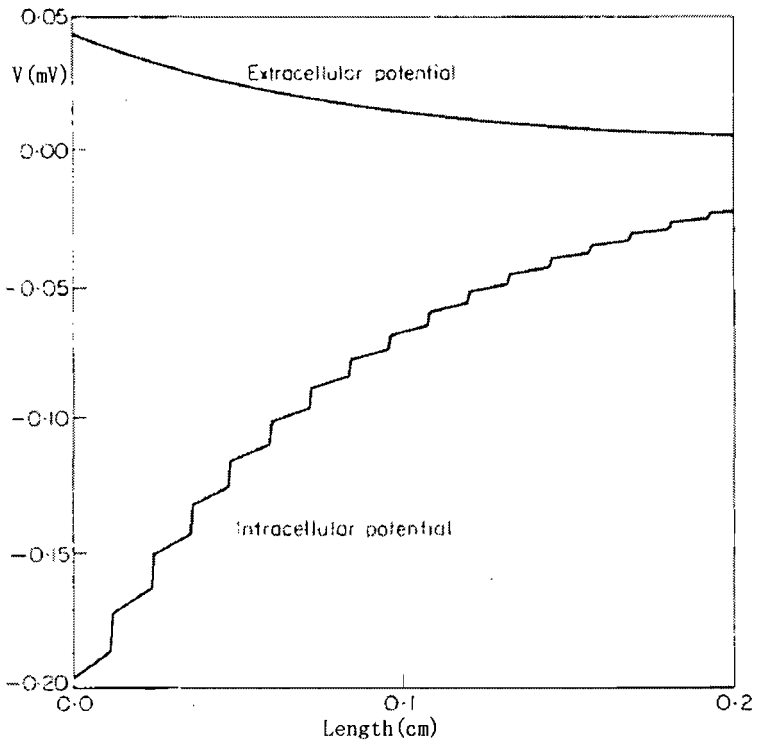

Figure 1.16: The intracellular potential and the extracellular potential are a function of the distance in the cell x [69].

the velocity between cells decreases with the increase in disk resistance as a result of an increased time delay at the disk. The intercellular latency increases because the current flowing from one cell to another is smaller as the gap junction resistance is increased, so that it takes longer for the next cell to reach threshold. Moreover, a slower increase of potential is also associated with a partial inactivation of the sodium current which further increases the threshold and the latency. This explains why there is a limiting value of intercellular gap resistance when propagation fails. As for the low longitudinal resistivity, the net macroscopic velocity closely follows the inverse square root relationship of continuous cable theory. However, in the case of high longitudinal resistivity, changes in the disk resistance result in a greater decrease in macroscopic velocity than predicted by the inverse square root relation [73]. Critical gap junction uncoupling reduces conduction velocities to a much larger extent than does a reduction of excitability, which suggests that the safety for conduction is higher at any given conduction velocity for gap junction uncoupling. In uniformly structured

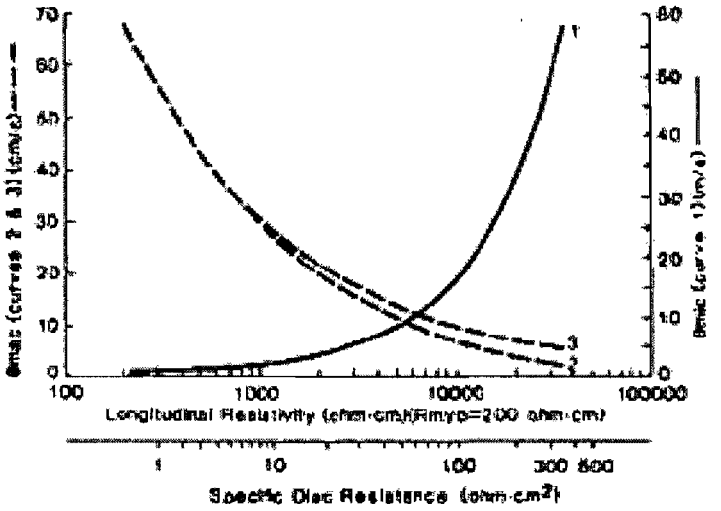

Figure 1.17: Effects of variations in axial (longitudinal) resistivity on velocity in cell (θ_{mic}, curve 1) and on average velocity between cells (θ_{mac}, curve 2). The continuous case (no disks included in the model) is shown for comparison (curve 3) and follows the inverse square root relation of continuous cable theory. The effective longitudinal resistivity is varied by varying the disk resistance while the myoplasm resistivity is kept constant at 200 $\Omega \cdot cm$. Both effective longitudinal resistivity and the corresponding disk resistance are indicated [73].

tissue, gap junction uncoupling is accompanied by a parallel decrease in conduction velocity. However, this is not necessarily the case for non-uniform structures like tissue expansion where partial uncoupling paradoxically increases conduction velocity and has the capacity to remove unidirectional conduction blocks [68, 70].

In a continuous cable of intracellular resistance R_i, the speed of propagation is proportional to $\sqrt{1/R_i}$. In a discrete cable, the global speed of propagation depends simultaneously on the gap resistance (as shown in Fig. 1.17) the intracellular resistiviy and the length of the cell (as shown in Fig 1.19). Joyner [71] has studied propagation in a cable stimulated from rest with membrane currents represented by the BR model. Each segment of the cable, with a length of 50 μm and a radius of 10 μm, has either a low axial resistivity $\rho_L = 200\Omega \cdot cm$ or a high axial resistivity ρ_H. He studied the situation depicted in the top panel of Fig. 1.20, where a single segment of high resistivity is intercalated between every island of N segments

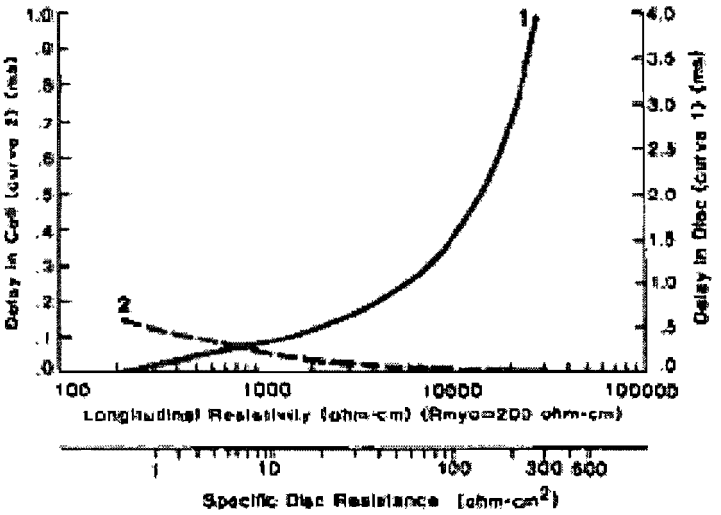

Figure 1.18: Delay of the propagating action potential as a function of disk resistance, both in the cell (curve 2) and at the intercalated disk (curve 1) [73].

of low resistivity. The equivalent lumped resistivity of the medium is then:

$$R_i = N\rho_L + \rho_H \tag{1.40}$$

The bottom panel of Fig. 1.20 shows the conduction velocity for the continuous media (A) and two levels of ρ_H, 5000 $\Omega \cdot cm$, (moderate, B) and 10000 $\Omega \cdot cm$ (high, C). The plot is given as a function of $\frac{R_i}{\rho_L} = N + \frac{\rho_H}{\rho_L}$, for different value of N [71]. For moderate discontinuity (B), the speed is always lower than for a continuous cable with equivalent lumped resistivity. For high discontinuity (C), the speed is lower than in (B), but has a maximum at an intermediate value of N. Although this setting does not represent a cell separated by discrete gap junction resistance (all segments have an active membrane), it shows that the velocity of propagation may depend, in a complex manner, on the distribution of the high and low resistive segments.

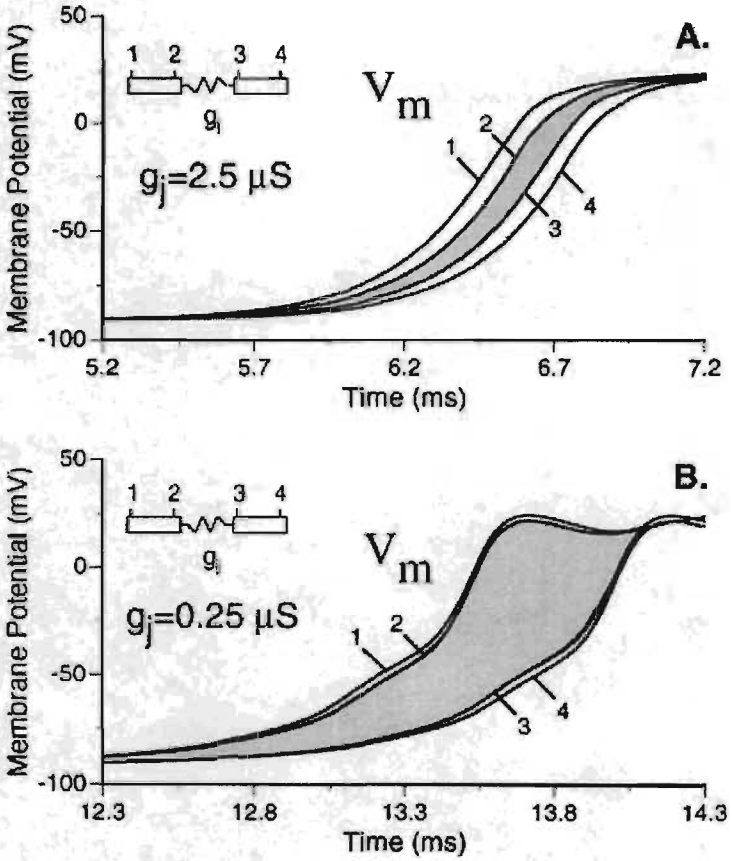

Figure 1.19: Increase in intercellular conduction delay with decrease in gap junction coupling. Action potential upstrokes from the edge elements (see inset) of two adjoining cells for intercellular conductance of $2.5\mu S$ (A) and intercellular conductance of $0.25\mu S$ (B). Discretization of 21 patches per cell was used. For control coupling (A), intercellular conduction delay is approximately equal to intracellular (myoplasmic) conduction time. A 10-fold decrease in intercellular conductance (B) increases intercellular conduction time and decreases intracellular conduction time dramatically, resulting in gap junction dominance of overall conduction velocity [70].

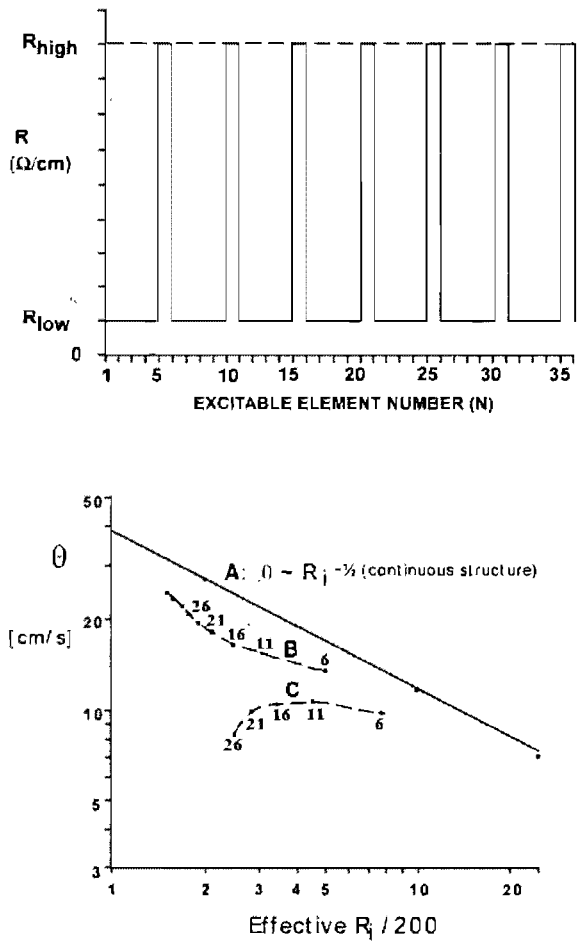

Figure 1.20: Principles of discontinuous propagation. Top: discontinuity is defined by a row of excitable elements (abscissa denotes element number) separated by resistors. N elements forming a group are interconnected by resistors of low value (R_{low}). Each group of N elements is connected to the next group by a resistor of high value (R_{high}). The effective or overall longitudinal resistance (R_i) plotted in the bottom panel is equal to the average longitudinal resistance. Bottom: change of propagation velocity (θ) as a function of R_i for 3 degrees of discontinuity. For simplicity, values are plotted in units of $R_i = 200\Omega \cdot cm$. Case A: continuous case, $\theta^2 \propto 1/R_i$ [72]. Case B: moderate discontinuity, $R_{low} = 200\Omega \cdot cm$, $R_{high} = 5,000\Omega \cdot cm$, the numbers on the trace denote the number of elements N in a group. Case C: marked discontinuity, $R_{low} = 200\Omega \cdot cm$, $R_{high} = 10,000\Omega \cdot cm$, the numbers on the trace denote the number of elements N in a group. Note that case B behaves similarly to the fully continuous case A. In case C, the propagation velocity decreases with both a large and a small number of elements N and is optimal only in a region where there is a match between R_{low}, R_{high}, and N [71].

Chapter 2

Dynamics of Sustained Reentry in a Loop Model with Discrete Gap Junction Resistance

This chapter, which presents the results of the reseach, is consisting of the scientific paper that has been submitted to the journal Phys. Rev. E on March 29, 2007, and published on Phys. Rev. E **76** 021928 (2007).

by Wei Chen, and the doctors Mark Potse and Alain Vinet

Abstract

Dynamics of reentry are studied in a one dimensional loop of a model of cardiac cells with discrete intercellular gap junction resistance (R). Each cell is represented by a continuous cable with ionic current given by a modified Beeler-Reuter formulation. For R below a limiting value, propagation is found to change from period-1 to quasiperiodic (QP) at a critical loop length (L_{crit}) that decreases with R. Quasiperiodic reentry exists from L_{crit} to a minimum length (L_{min}), which is also shortening with R. The decrease of $L_{crit}(R)$ is not a simple scaling, but the bifurcation can still be predicted from the slope of the restitution curve giving the duration of the action potential as a function of the diastolic interval. However, the shape of the restitution curve changes with R. An increase of R does not seem to increase the number of possible QP solutions since, as in the continuous cable, only two QP modes of propagation were found despite an extensive search through alternative initial conditions.

2.1 Introduction

Self-sustained propagation of electrical activity around a one-dimensional (1-D) loop of cardiac tissue is the simplest model of reentry, the mechanism by which a propagating activation front maintains itself by travelling around a functional or anatomical obstacle. Reentry has been much studied because it was demonstrated to be an important mechanism of cardiac arrhythmia [5,6,8,75]. For the 1-D loop, most work has been done assuming the membrane to be a continuous and uniform cable with constant intracellular axial resistivity [25,27–36]. For different models representing the ionic properties of the membrane, propagation was found to change from stable period-1 propagation to quasiperiodic reentry when the length of the loop was reduced below a critical length. The quasiperiodic reentry was characterized by a spatial oscillation of the action potential duration as propagation proceeded around the loop. Based on numerical simulations, the bifurcation was in most cases classified as supercritical, with the amplitude of the oscillation growing as the length of the loop was reduced below the critical length. Quasiperiodic reentry was found to exist from the critical length to a minimal length below which sustained propagation became impossible. In some instances, two different modes of quasiperiodic propagations were identified, with different wavelengths, different intervals of existence, and sometimes different scenarios of creation [25, 27, 29–31]. Various attempts were made to build simplified representations of the dynamics allowing analytical examination of the nature of the bifurcation [29, 32, 38, 76, 77]. One of these approaches, which guides the present investigation, relies on an integral-delay model [30, 31]. It is based on the assumption that both the speed of propagation and the action potential duration can be expressed as functions of the diastolic interval, which measures the recovery time from the end of the previous action potential. The model has been successful in reproducing the locus of the bifurcation observed by numerical simulations of 1D loops with Beeler-Reuter-type representations of the membrane. It predicts that the bifurcation should occur when the diastolic interval in the period-1 reentry reaches the critical value where the slope of the restitution curve becomes 1.

However, cardiac excitable tissue is not a syncytium, but rather a mesh of myocytes connected by discrete gap junction resistances [78]. Much work has been done to investigate the effect of discrete resistances in a one-dimensional structure [35, 69, 70, 79–81], many focused on the effect of resistivity on excitability. In the discrete case, the resistance no longer acts as a scaling factor with regard to space. Because the intercellular current is reduced as the gap junction resistance is increased, the latency of the cell-to-cell propagation is augmented until propagation fails at some limiting value of the resistance. Besides, upon premature or repetitive stimulations, the excitability of the tissue must be more recovered for propagation to proceed, which corresponds to an increase of the refractory period. Discrete coupling has also been to shown to act on the dynamics of propagation during reentry and pacing by modifying the repolarization, thereby changing the duration of the action potentials [88–90].

This paper describes how the bifurcation from period-1 to quasiperiodic propagation and the characteristics of the quasiperiodic propagation are modified by the increase of the intercellular resistance in a 1D loop of discrete model cardiac cells. This paper is organized as follows. In the next section, the model and computational method are described. The results of the numerical simulation are presented in 2.3. The bifurcation from stable period-1 reentry is explained in 2.4. The QP modes of reentry are analyzed in 2.5. The final section is devoted to a summary and discussion.

2.2 Methods

We consider a one-dimensional loop formed by N identical cells connected by gap junction resistances. Each cell is modeled as a continuous and uniform cable of radius (a) 5 μm, length (L_c) 100 μm and intracellular resistivity (ρ) 0.2 $K\Omega \cdot cm$ lying in an unbounded volume conductor of negligible resistivity. The transmembrane potential ($V^{i=1,N}$ in mV) of the cells is described by the well-known cable equation:

$$\begin{aligned} \frac{1}{\rho}\frac{\partial^2 V^i(x,t)}{\partial x^2} &= S[C_m\frac{\partial V^i(x,t)}{\partial t} + I^i_{ion}(x,t)], \\ x &\in \{0, L_c\}\,,\ i \in \{1, N\} \end{aligned} \tag{2.1}$$

in which C_m is the membrane capacitance ($1\ \mu F/cm^2$), S is the surface-to-volume ratio ($0.4\ \mu m^{-1}$) and I_{ion} is the ionic current ($\mu F/cm^2$). The membrane ionic model is the same MBR model that was used in our previous works on continuous 1D and 2D rings [23, 27, 29, 39, 82]. In this model, the sodium current is controlled by an activation gate variable m and two inactivation gate variables h and j. The plateau and repolarization of the action potential involve a gate controlled calcium current as well as a gate controlled and a voltage dependant potassium current. Each cell is connected to its neighbors by a discrete gap junction resistance R ($K\Omega$). Continuity of the intracellular current between the cells yields the boundary conditions [69]

$$\begin{aligned} \frac{\partial V^i}{\partial x}|_{x=L_c} &= \frac{\partial V^{mod(i,N)+1}}{\partial x}|_{x=0} = -\frac{\rho}{\pi a^2} I_{i,mod(i,N)+1} \\ V^i(L_c) &- V^{mod(i,N)+1}(0) = R I_{i,mod(i,N)+1} \end{aligned} \tag{2.2}$$

For simulation, we have modified the numerical method that we developed for continuous loops [27]. Briefly, for each time step ($\Delta t = 2\ \mu s$), Eq.(2.1) becomes equivalent to an ordinary differential equation

$$\frac{d^2 V^i(x)}{dx^2} - K^2 V^i(x) = g^i(x) \tag{2.3}$$

whose solution can be expressed as the sum of a particular solution $V^i_p(x)$ and of the homogeneous solution

$$V^i_h(x) = A_i e^{kx} + B_i e^{-kx} \tag{2.4}$$

$V^i_p(x)$ is obtained by solving Eq.(2.3) with Neumann boundary conditions ($\partial V^i/\partial x|_{x=0,L_c} = 0$) using a Galerkin finite element method projected on linear basis function [34] with a

uniform grid ($\Delta x = 25\mu m$), i.e. five nodes. Cells are then reconnected by choosing the coefficients of the homogeneous solutions to fulfill the continuity conditions given by Eq.(2.2). For a subset of R values, calculations repeated with $\Delta x = 12.5\mu m$ and $\Delta t = 1\mu s$ gave the same results.

The purpose of the simulations is to obtain a description of the regimes of reentry of the function R and $L = NL_c$, the length of the loop. During reentry, the successive action potentials ($s = 1, l$) at each node can be characterized by their activation times (T^s_{act}), set at the maximum derivative of the upstroke, and their repolarization times (T^s_{repol}), taken at the -50 mV downcrossing in repolarization. The action potential duration (A) and the diastolic interval (D) associated to each action potential are calculated respectively as $A^s = T^s_{repol} - T^s_{act}$ and $D^s = T^s_{act} - T^{s-1}_{repol}$ [25, 27–29]. The propagation of the wave front along the loop generates spatial profiles of A and D that typify the reentry. In contrast to a continuous loop, propagation on a discrete loop can be patterned inside each cell but identical across all the cells. We have chosen to use only A and D values of the middle node of all cells to characterize the reentries. We label period-1 (P-1) reentries in which A and D remain constant across all the middle nodes, and QP reentries where A and D oscillate both in time and space. The label "quasiperiodic" was used by analogy with the results of the analysis of integral-delay model done by Courtemanche et al. [30,31], but no further processing was done to clarify the exact nature of these nonconstant solutions.

For each value of R, an initial L was chosen large enough to sustain P-1 stable reentry. Reentry was initiated by transiently opening the loop and stimulating one end. Computation was continued until stable period-1 reentry was detected, the stability criteria being less than 0.5 ms difference in A and D between all the middle nodes for one rotation of the front. Afterward, the loop length was gradually reduced by steps of one cell, using the final state of the previous L as initial condition and removing one cell far from the position of the excitation front. When the stability criterion was not fulfilled after a minimum of 25 turns, reentry was labelled as QP. With this procedure, both L_{crit} and P_{crit}, respectively, the minimum length

and minimum period with P-1 reentry, as well as L_{min}, the minimum length for sustained reentry, were identified for each value of R. In some instances, bistability between P-1 and QP reentry was investigated by stepwise expanding loops that were initially in quasiperiodic regime. One cell was inserted in the loop, with initial conditions set at the mean of the states of its neighboring cells. Finally, we also searched for distinct modes of QP reentry using the method described in [29], in which D spatial profile of a QP solution for a given L value is compressed by a scaling factor to construct initial conditions to find alternative QP solutions with smaller wavelengths.

2.3 Results

Figure 2.1 A) shows L_{crit} and L_{min} as a function of R. Both L_{crit} and L_{min} decrease until they merge at $R \simeq 104\ K\Omega$. From this resistance, QP reentry does not exist anymore and P-1 reentry remains the only regime of sustained propagation. From there, the limiting length for P-1 reentry increases until sustained propagation becomes impossible at $R \simeq 108.429\ K\Omega$. Increasing the resistivity in a continuous loop would also decrease L_{crit} and L_{min}. However, the speed of propagation being proportional to $1/\sqrt{\rho}$ in a continuous media [83], $\sqrt{\rho}L_{crit}(\rho)$ and $\sqrt{\rho}L_{\min}(\rho)$ would remain invariant. To compare the continuous and discrete medium, we computed the equivalent resistivity of the latter as

$$\rho_{eqv}(R) = \rho + \frac{NR\pi a^2}{L} = \rho + \frac{R\pi a^2}{L_c} \tag{2.5}$$

With this notation, $R = 0$ corresponds to a continuous loop with resistivity ρ. If the two media were equivalent, the ratio $L(R)\sqrt{\rho_{eqv}(R)}/L(R=0)\sqrt{\rho}$ would remain equal to 1. Fig. 2.1 B) shows clearly that the diminution of L_{crit} and L_{min} cannot be explained by a simple scaling, as it occurs in a continuous medium.

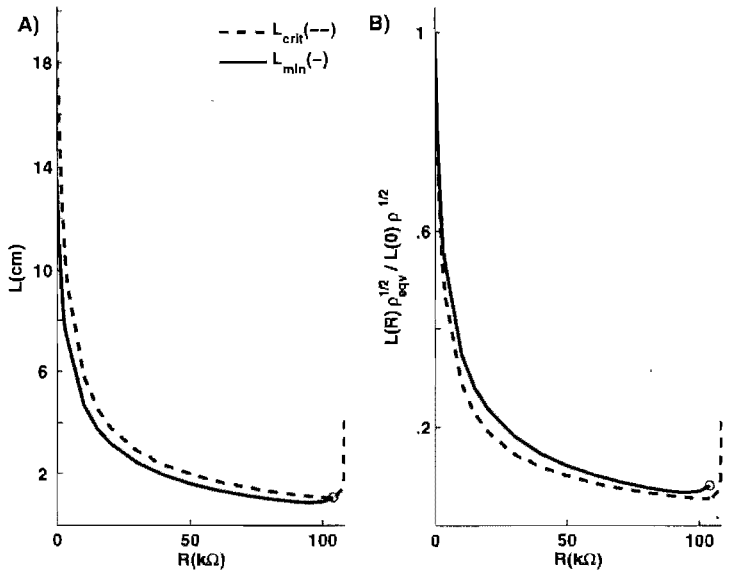

Figure 2.1: A) L_{crit} (cm, dashed line), the shortest L with period-1 reentry, and L_{min} (cm, solid line), the mininum L with QP reentry, as a function of the gap resistance $R(K\Omega)$. B) Normalized values of L_{crit} and $L_{min} = L_{crit,min}(R)\sqrt{\rho_{eqv}(R)}/L_{crit,min}(R=0)\sqrt{\rho}$ (see text).

2.4 L_{crit}, P_{crit} in transition to QP reentry.

Two distinct scenarios can lead to the disappearance of P-1 reentry. For $108.429K\Omega > R > 104K\Omega$, sustained reentry does not exist for $L < L_{crit} = L_{min}$, so that reentry ends abruptly with the disappearance of the P-1 solution. For $R < 104K\Omega$, P-1 reentry is replaced by QP reentry that persists from L_{crit} to L_{min}. In this section, we consider the second type of transition. In the continuous MBR loop, the bifurcation from P-1 to QP propagation occurs at the critical period $P_{crit} = D_{crit} + A_{crit}$ where D_{crit} and A_{crit} are the values for which the slope of the restitution curve $A(D)$ reaches 1 [27, 30]. P_{crit} is constant and independent of ρ in a continuous medium. In contrast, Fig. 2.2A) shows that P_{crit} increases with R in the discrete loop. Both A_{crit} and D_{crit} contribute to the change of P_{crit} (Fig. 2.2B), but the increase of D_{crit} is more important. For each value of R, we collected the D and A values of the P-1 solutions for a set of L values close to L_{crit} as well as those of the first QP solution below L_{crit} to construct the $A(D)$ restitution curve. Each curve was fitted with a simple exponential to find $D_{crit,th}(R)$, the value where the slope of the fitted $A(D) = 1$, and the

theoretical value $P_{crit,th} = D_{crit,th} + A(D_{crit,th})$. As shown in Fig. 2.2A, $P_{crit,th}$ falls very close to the P_{crit} values found by simulation. Hence, the mechanism responsible for the transition from P-1 to QP reentry is the same in the continuous and discrete loop, and the increase of P_{crit} results from R transforming the restitution curve. The mechanisms responsible for the change of D and A can be identified in Fig. 2.3, which shows the action potentials of the first node in the three successive cells for increasing values of R. (top to bottom, R=0, 80 and 103 $K\Omega$). Increasing R prolongs the latency of the action potential, defined as the time interval between the minimum diastolic potential and the beginning of the action potential, set at the maximum derivative in the upstroke (left column panels). Since latency is included in the diastolic interval, its increase translates as an increase of D.

The mechanisms responsible for the change of A_{crit} and of the form of the restitution curve are complex and involve an interaction between the diffusive current and the gate variables, as it has been demonstrated in previous works [88, 90]. Neighboring cells exchange current during the early phase of repolarization, which compensates for the delay of activation and tends to prolong the action potential. If the time course of the gate variables of the calcium and potassium currents controlling the action potential duration was not concurrently altered during the subthreshold and early repolarization phase, $A_{crit}(R)$ would always be longer than $A_{cont}(D_{crit}(R))$, the duration of the action potential produced by an activation with $D = D_{crit}(R)$ on a continuous loop. As illustrated Fig. 2.2B), $A_{crit}(R)$ is always smaller that $A_{cont}(D_{crit}(R))$, which shows that the net effect of the diffusion current goes beyond a simple passive prolongation of the action potential.

Once P_{crit} is known, L_{crit} can be calculated if the speed of propagation $\theta(D_{crit})$, is provided. In discrete media, the total time to propagate from one cell to another is a composite of the propagation time within and between the cells. The former decreases with R , while the latter, which is equivalent to the latency displayed in Fig. 2.3, increases. The final composite $\theta(D_{crit}(R))$ is shown in left panel of Fig. 2.4. In a continuous medium, $\theta_o(D)\sqrt{\rho} = c(D)$, where $c(D)$ is constant characterizing each value of D and $\theta_o(D)$

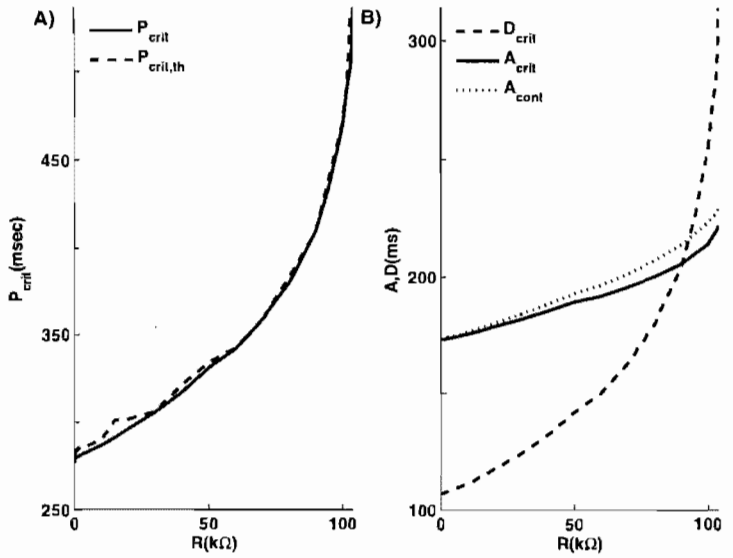

Figure 2.2: A) Solid line: For each value of the gap resistance R, the critical cycle length P_{crit} (ms) at L_{crit}, the shortest loop with period-1 reentry. Dashed Line: $P_{crit,th}$, the critical cycle length computed from the restitution curve (see text). B) Value of diastolic interval (D_{crit}, dashed line) and of the action potential duration (A_{crit}, solid line) at L_{crit}. The dotted line (A_{cont}) is the action potential duration for P-1 solutions with $D = D_{crit}(R)$ on the continuous cable.

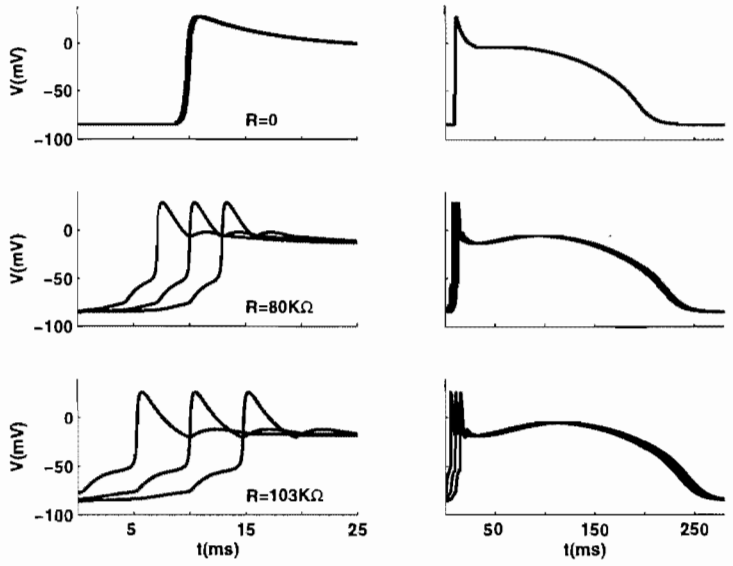

Figure 2.3: Action potentials (mV) in the first node of 3 successive cells as a function of time (ms) during period-1 reentry for, from top to bottom, $R = 0$, 800 and 103 $K\Omega$. In the left column panels, only the activation is shown, while the complete action potentials are displayed in the rigth column panels.

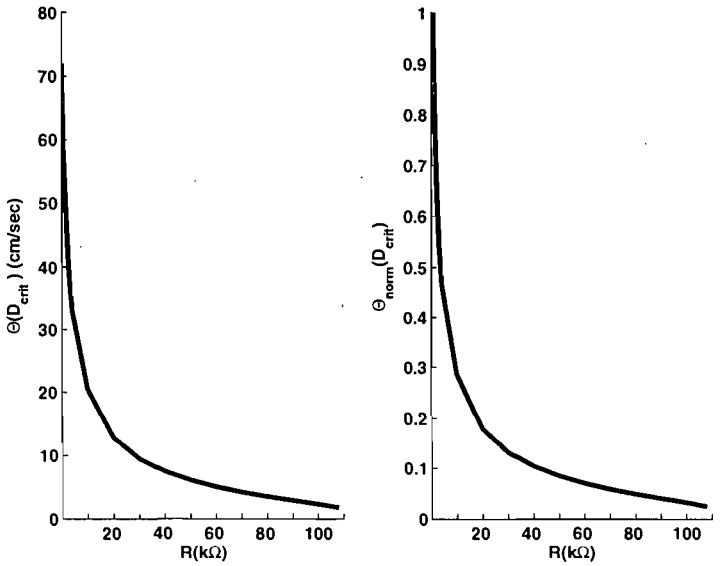

Figure 2.4: Left panel: $\theta(D_{crit})$ the intercellular activation speed (calculated between the first node of successive cells, cm/s) at D_{crit} as a funtion of the gap resistance R. Right panel: $\theta_{norm}(D_{crit})$, normalized activation speed, defined as $\theta(D_{crit}(R))\sqrt{\rho_{eqv}(R)}/\theta_0(D_{crit}(R))\sqrt{\rho}$, where $\theta_0(D)$ is the speed of a period-1 solution with diastolic interval D in the continuous loop.

refers to the speed of a period-1 solution with diastolic interval D. Hence, $\theta_{norm}(D_{crit}(R))=$ $\theta(D_{crit}(R))\sqrt{\rho_{eqv}(R)}/\theta_0(D_{crit}(R))\sqrt{\rho}$ would remain equal to 1 if R was acting on the speed only as a scaling factor, which is not the case as shown in the right panel of Fig. 2.4.

2.5 QP reentry

The characteristics of the QP reentry in the continuous MBR loop have been extensively discussed in previous papers [27]. Two modes of QP were identified, characterized by D and A oscillations with different spatial wavelengths (λ). The first mode, referred to as mode-0, exists from L_{crit} to L_{min}. Its λ, close to two turns of the loop at L_{crit}, diminishes as the loop is shortened, but always remains longer than L. It appears through a supercritical bifurcation, in which the amplitude of D and A oscillation grows from zero as L is decreased below L_{crit}. The second, referred as mode-1, exists only over a subset of the $[L_{min}, L_{crit}]$ interval with λ always less than L. The mode-1 solution is created by a subcritical bifurcation at $L < L_{crit}$.

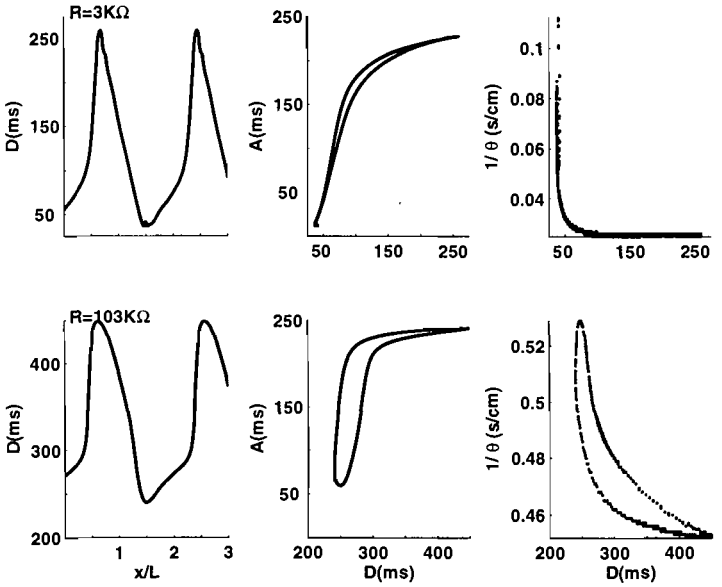

Figure 2.5: Characteristics of the mode-0 QP solution at L_{min} for $R = 3K\Omega$ (top row panels) and $R = 103K\Omega$ (bottom row panels). Left panels: D, the diastolic interval, as a function of position (x/L) for three successive turns abutted end-to-end. Middle panels: A, the duration of the action potential, as a function of D, from the solutions shown in the left panels. Right Panels: $1/\theta$, the cell-to-cell conduction time, as a function of D from the solutions shown in the left panels. Only the data of the first node of each cell were used to construct these plots.

These two types of QP solutions were found for all values of $R < 104K\Omega$ where QP solutions exist.

2.5.1 mode-0 QP reentry

We first consider the mode-0 solutions that exist over the whole $[L_{min}, L_{crit}]$ interval. Fig. 2.5 presents the characteristics of the mode-0 solutions at L_{min} for two values of R (top panels , $R = 3K\Omega$, $L = 7.65cm$, bottom $R = 103K\Omega$, $L = 1.04cm$). The leftmost panels show the spatial oscillation of D by plotting successive turns end to end. Similar mode-0 solutions were obtained for all $L \in [L_{min}(R), L_{crit}(R)]$, characterized by stable D spatial profiles repeating with a wavelength $\lambda > L$. These solutions can be either periodic or quasiperiodic, depending whether λ is a rational or irrational fraction of L. Since λ decreases gradually as L is reduced, we chose to refer to them collectively as mode-0 quasiperiodic solutions.

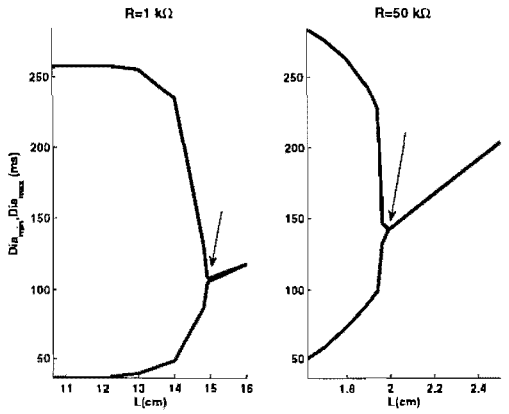

Figure 2.6: D of the period-1 solution and from $L = L_{crit}$ (arrow) $D_{\max}$ and $D_{\min}$ of the mode-0 QP solution as a function of L for R =1 $K\Omega$ (left panel) and 50 $K\Omega$ (right panel).

Mode 0 solutions were also found to appear through a supercritical bifurcation with, as shown in Fig. 2.6, a gradual increases of the amplitude below L_{crit}. For these two cases, the nature of the bifurcation was further ascertained by prolonging the calculation up to 100 turns for L values close to L_{crit} and by enlarging the loop starting from $L < L_{crit}$ in the mode-0 QP regime.

An obvious difference between the left column panels of Fig. 2.5 and between those of Fig. 2.6 is the range of D values covered by the solutions for different R. The left panel of Fig. 2.7 shows D_{min} and D_{max}, the minimum and maximum value of D for the mode-0 solutions at $L_{min}(R)$. It is well known that, in a discrete medium, the minimum excitability needed to sustain propagation increases as a function of R until a limiting value beyond which propagation is blocked even in a medium at rest [80]. In the MBR model, the excitability can be measured by the product hj of the inactivation gates of the sodium current. The right panel of Fig. 2.7 shows $hj(D_{min})$ and $hj(D_{max})$, the excitability of the action potentials produced, respectively, at D_{min} and D_{max} for the mode-0 solutions at L_{min}. As R increases, the minimal excitability allowing propagation becomes higher, which requires an increase of $D_{min}(R)$. At $R = 104K\Omega$, $hj(D_{min}) = hj(D_{crit})$, QP propagation disappears and only P-1 reentry remains. On the other hand, the curve $hj(D_{max})$ rather reflects the inactivation of the sodium current occurring during the latency preceding the

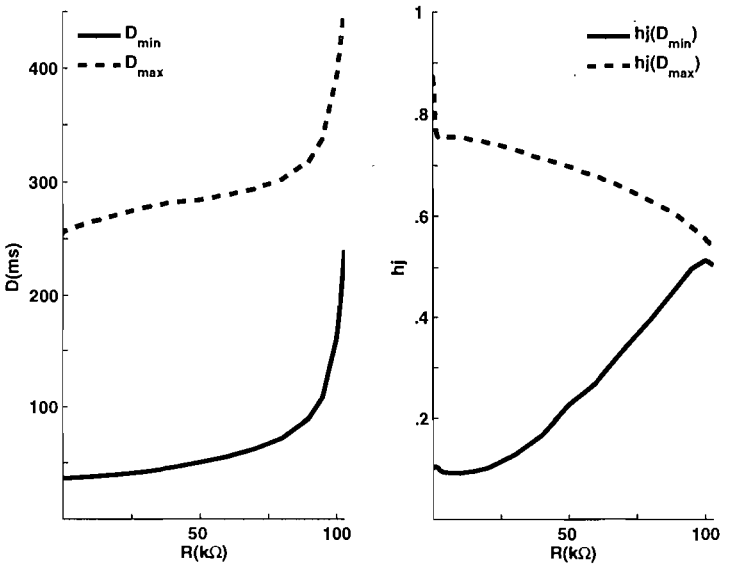

Figure 2.7: Left Panel: D_{min} (solid line) and D_{max} (dashed line), respectively, the minimum and maximum diastolic intervals of the mode-0 QP solutions at L_{min} as a function of R. Right Panel: hj, the product of the sodium current inactivation gates taken at D_{min} (solid line) and D_{max} (dashed line) for the mode-0 QP solutions at L_{min}.

upstroke of the longer action potential. At $R = 104K\Omega$, the limit for QP propagation, $hj(D_{max}) > hj(D_{min}) = hj(D_{crit})$, which indicates that P-1 propagation is still possible if R is increased. However, the difference is small, such that the range of R values over which P-1 reentry can still occur is limited, as it is seen in Fig. 2.1.

The middle column panels of in Fig. 2.5 display the $A(D)$ relation obtained from each QP mode-0 solution. Each curve has two branches, the lower and upper branch coming, respectively from the increasing and the decreasing portion of the D spatial profile. Such a dual structure has been observed in the continuous loop and was explained either by the influence of neighbors on the repolarization [38] or by short term memory [36]. The separation between the branches is enhanced by the increase of R. Finally, the right column panels of Fig. 2.5 show $1/\theta$ vs D, the dispersion relation of the conduction time. For $R = 3K\Omega$ (top right panel), the dispersion relation appears as a single value function, similar to what is seen in the MBR continuous loop. For $R = 103K\Omega$ (bottom right panel), the dispersion relation has two branches, as the $A(D)$ curve. The lower branch is associated with the decreasing

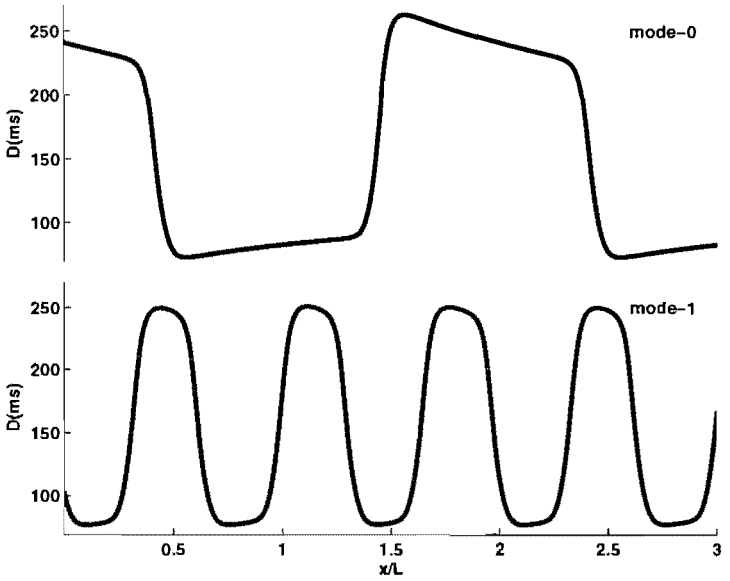

Figure 2.8: Mode-0 (top panel) and mode-1 (bottom panel) QP solutions for L =1.80cm and R =50$K\Omega$. The plots show D, the diastolic interval, as a function of position (x/L), for three turns abutted end to end.

portion of the D spatial profile.

2.5.2 Higher QP Modes

Fig. 2.8 shows an example of mode-0 and mode-1 solution for $R = 50K\Omega$ and $L = 1.8$ cm, in the middle of the $[L_{min}, L_{crit}]$ =[1.61cm, 1.99cm] interval for this value of R. Mode-1 solutions were found for all values of R with QP propagation over a subset of the $[L_{min}, L_{crit}]$ interval, as in the case of the continuous cable. Courtemanche et al. [31] in their analysis of a delay-integral model representing reentry on a 1D loop have predicted the existence of an infinite number of QP modes, with spatial wavelengths near L_{crit} given by

$$\lambda(n) = \frac{2L}{2n+1} - \frac{C}{(2n+1)^3} \tag{2.6}$$

where n is the order of the mode and C is a small positive constant. As seen Fig. 2.8, $\lambda(0)/\lambda(1)$ is indeed close to 3. However, in the MBR continuous loop, only the first two modes (i.e. 0 and 1) were observed. This was explained by the effect of resistive coupling between neighbors that limits the spatial gradient of voltage and forbids the appearance of

higher modes [29]. Theoretically,

$$\frac{\lambda(2)}{\lambda(0)} \simeq \frac{1}{5}, \qquad \frac{\lambda(2)}{\lambda(1)} \simeq \frac{3}{5}. \tag{2.7}$$

To look for mode-2 solutions for different R and L values, we have compressed the D profiles of the mode-0 and mode-1 solutions up to, respectively, a factor 6 and 2 to build different initial conditions. This procedure was successful in obtaining mode-1 solutions from mode-0 solutions, but higher modes of propagation were never produced. For all scaling factors, propagation was found to stabilize either to mode-0 or mode-1. It is noteworthy that mode-1 solutions always appeared at $L < L_{crit}$ with a high-amplitude complex oscillations that damped as L was reduced, until reaching smooth patterns as the one shown in Fig. 2.8.

2.6 Discussion and Summary

Increasing R in the discrete loop allows sustained reentry to be maintained in much shorter circuits than in continuous loops with equivalent lumped resistance. The critical period at which the bifurcation from period-1 to QP propagation occurs can still be predicted from the $A(D)$ dispersion curve constructed by gathering data from P-1 solutions and from mode-0 QP solutions close to the supercritical bifurcation. However, increasing R modifies $A(D)$ and the value of P_{crit}. On one hand, the latency of the cell to cell propagation is augmented due to the decrease of the intercellular current. This prolongs D , which includes the latency, and pushes $A(D)$ to the right. The partial closure of the sodium current inactivation gates, which occurs during slow depolarization, increases the voltage threshold and also contributes to the prolongation of D. In space-clamped models, changing the amplitude [88] or the duration of square pulse stimuli [91] modifies the $A(D)$ restitution curve. Hence, the change of the subthreshold depolarization coming with higher R impacts on the restitution curve, together with the diffusion current in early repolarization phase that influences the time course of the membrane voltage and of the gate variables. The increase of P_{crit} and the change of $A(D)$ are in line with the results of Qu [88] who found, using a Luo-Rudy-1 paced cable with nodes

linked by discrete resistances, that reducing the coupling displaced the onset of alternants toward higher stimulation periods.

The shift of P_{crit} depends on both the change of D_{crit} and $A(D_{crit})$. In order to analyze these effects, it would be more appropriate to separate the latency from the diastolic interval, redefining D from the end of the action potential to the minimum of V in repolarization and considering the latency lat to extend from the end of D to the maximum derivative of the upstroke [92]. Then both A and lat could be analyzed as functions of D and R. However, even with this change, it will be difficult to build a low-dimensional equivalent model of the propagation, extending the integral-delay model developed for the continuous loop. As seen in Fig. 2.5, increasing R enhances the dual structure of $A(D)$ during propagation. Moreover, a similar type of dual structure also appears for $1/\theta$, which is almost equivalent to the latency at high R values. It thus becomes impossible to neglect the modulating effect of coupling on both A and θ at high R values. Whether alternative approaches that have been proposed for the continuous loop would be more appropriate remains to be determined [32,76,77]. In any case, we are still far from a general low-dimensional model that could also be applied in situations including a dynamic change of the intercellular coupling, as in [84–86].

R also influences L_{min}, the minimal length with QP propagation. Because higher R necessitates more excitability for propagation, the minimum D in sustained QP reentry increases until it reaches $D_{crit}(R)$. From this value of R, QP propagation becomes impossible. For R above this limiting value, period-1 reentry ends abruptly when its D reaches the minimal value allowing propagation. The minimal L for propagation increases until R reaches the value where propagation becomes impossible even in a medium at rest. Again, it would be very interesting to study reentry in a medium with dynamical modulation of the gap resistance.

In all cases with QP propagation, we found the bifurcation from period-1 to mode-0 propagation to be supercritical. For some R values, the nature of the bifurcation was further ascertained by prolonging simulation up to 100 rotations and by expanding the

loop from a length with QP propagation. It cannot be excluded that the bifurcation was misclassified at least for some values of R because of prolonged slow growing transients. A numerical analysis of an integral-delay model of reentry has shown that increasing the slope of the $A(D)$ function could turn the bifurcation from super to subcritical [29]. Since Qu [88] has reported that reduced coupling increases the slope of $A(D)$ at least at short D values and since Fig. 2.5 also shows that it increases the steepness of the restitution relation, the increase of R was expected to change the bifurcation. However, the nature of the bifurcation, which is determined by the response of the system to small perturbations around the period-1 solution, is controlled by the variation of the slope close to D_{crit}. In our case where the $A(D)$ functions were constructed from stable solutions close to $L_{crit}(R)$, we observed a minimal increase of the steepness of the function around D_{crit} for all values of R. This may explain why the bifurcation has remained supercritical, and it does not exclude the possibility that it could be different for other ionic models.

As in the continuous case, the mode-1 solutions were found to exist in a subset on the $[L_{min}, L_{crit}]$ interval. We also devoted much effort to finding $n > 1$ modes of QP propagation for different values of R, building initial conditions either from mode-0 or mode-1 solutions for different L within the $[L_{\min}, L_{crit}]$ interval. All these attempts were unsuccessful. Our initial guess was that the increase of R should allow more abrupt gradients of potential to exist between the cells, thus permitting the existence of higher modes of propagation. However, as seen in Fig. 2.5 , the dual structure of the $A(D)$ and $1/\theta$ relations becomes more pronounced at high R. This suggests that coupling still limits the gradient below what would be needed for higher modes of propagation.

This work was supported by a grant from the Natural Sciences and Engineering Research Council of Canada.

Chapter 3

Discussion and Conclusion

In an isotropic continuous medium, the resistivity acts only as a space scaling factor such that the dynamics of the system is invariant once expressed in one-dimensional space and time coordinates. Our work shows clearly that this is the case in homogenous medium made of discrete cells connected by resistive gap junctions.

Increasing the gap junction resistance R in a one-dimensional discrete loop speeds up the propagation of the activation front within each cell, but increases the latency of the cell-to-cell propagation. Because the latter effect becomes more important as R is increased, the global macroscopic speed is much lower than in a continuous cable with equivalent lumped resistivity. As a consequence, sustained reentry can be maintained on much shorter loop than for continuous media. The effect of R on speed was already documented in previous work [68–70, 73, 74]. The intercellular potential is not continuous change with the length of tissue, and the propagation speed is not as $\theta \propto R^{1/2}$. The speed between cells decreases with R increasing, and the speed in the cell increases with R increasing.

R has also an effect on the repolarization and on the duration of the action potential. The difference of firing times between neighbouring cells mentioned above, results in a difference of potential between the cells at the beginning of their action potential as in Fig. 2.3. These differences of potential are partially erased by the current exchanged during repolarisation. As a consequence, the action potential duration, which is measured from the upstroke, is prolonged as R is increased. Longer latency also means that the raise of the potential toward

the threshold is slower, which implies a partial closure of the sodium current inactivation gates and an opening of the activation gate of the potassium current during the foot of the action potential. These two effects contribute together to a further raise of the threshold. As a consequence, the minimum excitability to sustain propagation must be higher as R is increased, which corresponds to a larger minimum diastolic interval $DIA_{min}(R)$. $DIA_{min}(R)$ increases until a limiting value of R where propagation becomes impossible even in a medium at rest where excitability is maximal.

Our work was focussed on two specific aspects of the reentry: the bifurcation from period-1 to QP reentry occurring at a critical length $L_{crit}(R)$; the regime of QP bifurcation existing for $L < L_{crit}$. For continuous isotropic one-dimensional loop, the stability of the period-1 reentry was shown to be controlled by the slope of the restitution curve. For a period-1 reentry on a loop of length L with diastolic interval $DIA_f(L) = const$ to be stable, the slope of the restitution curve at DIA_f has to be less than one. As a consequence, period-1 solutions lose stability at the critical diastolic interval DIA_{crit} where the slope of the restitution curve reaches the value of 1. This result was also proved analytically using an integral-delay model based on the premise that both the APD and the velocity are invariant functions of DIA. Our work shows that this is still true in the discrete loop model. However, since the restitution curve change with R, a representative restitution curve has to be obtained for each value of R.

One may questions the relevance of the integral-delay model since the restitution curve obtained in quasiperiodic reentry is multiple-valued for the continuous loop, and that this effect is even more marked in the continuous loop as in Fig. 1.10. However, it must be remember the argument, based on a linearization of the integral-delay model, concerns the response of the system to infinitesimal perturbations around the period-1 solution. In order to judge the stability of a specific $DIA_f(L)$ period-1 solution, what is needed is a restitution function representing realistically the fluctuation of APD resulting from small perturbations around $DIA_f(L)$. In the context of local stability, the fact that $APD(DIA)$ may not repre-

sent the response of the system for DIA far from $DIA_f(L)$ is inconsequential. In our case, representative restitution curves for each value of R, were obtained by using points coming from the stable period-1 solutions at values of L close to the critical length L_{crit} as well as those of the mode-0 solutions also close to L_{crit}, for which the variation of DIA curves only a few ms. This choice ends up being appropriate since it enables a correct prediction of the critical period P_{crit}. We suggest that this procedure will still be appropriate with ionic models with large memory effect, in which the restitution curve is built by premature stimulation changes according to the prior rhythm of stimulation [29].

The second aspect of our research was on the nature of the QP reentries existing between the critical length L_{crit} and the minimum length L_{min} with sustained reentry. We found the QP solutions to disappear at a critical value of R where $DIA_{min} = DIA_{crit}$. For R less than a critical value, we found two modes of QP reentries, similar to those observed in the continuous loop model. In the continuous loop model, it was suggested the presence of only two modes of reentry, the difference in the values of L where each mode was appearing, as well as their respective scenario of creation were explained by the effect of coupling on repolarization. This led to a modification of the integral delay model to include the effect of neighbours on repolarization which was reproducing all the dynamics of the MBR ionic loop model. As shown in figure 2.5, the effect of coupling on the repolarization in QP propagation becomes more important as R is increased. Besides, it also shows up on the dispersion curve of the macroscopic speed that also becomes multivalued, while this effect was negligible in the continuous loop. To extend the integral-delay model to reproduce correctly all the regimes of propagation for a specific value of R will thus at least necessitate obtaining representative restitution and dispersion functions, an appropriate value of DIA_{min}, and to develop a correct representation of the effect of neighbours on these two functions. The challenge will even be more complex for a reduced model that could be applied for all values of R. Our results show that APD, the speed and DIA_{min} are all changes as a function of R. Whether these changes can be realistically described by analytical expressions

remains to be seen. This will be a prerequisite for a low dimensional model that could be applied in the context of dynamically changing gap resistance, as it is known to be the case [85]. Their results show that, when the cells are tightly coupled (6700 channels), the gap junction resistance during propagation is few changes. Thus, for tight coupling, there are negligible differences in the waveshape and propagation velocity when comparing the dynamic and static gap junction representations. For poor coupling (85 channels), the gap junction resistance increases 33 $M\Omega$ during propagation. This transient change in resistance resulted in increased transjunction conduction delays, changes in action potential upstroke, and block of conduction at a lower junction resting resistance relative to a static gap junction model. The results suggest that the dynamics of the gap junction enhance cellular decoupling as a possible protective mechanism of isolating injured cells from their neighbors.

Future work should also extend this study to two and three dimensional tissue. Transition from period-1 to QP reentry has also been observed in continuous two dimensional annulus [39–42, 87]. In this case, it was shown that, besides the restitution curve, the bifurcation was dependant on the internal and external radius of the media, which both influence the curvature of the activation and repolarization front [39, 41]. A discrete annulus model will have to consider the evolution of the potential in both the axial and transverse direction within each cell. How our numerical method, which solves each cell with Newman boundary condition and reconnected them by using the homogeneous solutions of the system, can be adapted to a two-dimensional setting?

In summary, numerical simulations have provided us a complete quantitative description of the regime of reentries on a one-dimensional loop model. The low-dimensional representation developed for the continuous loop model was useful to understand the variation of L_{crit} as a function of R, as well as the reduction and final disappearance of the interval of L over which QP solutions could exist. However, it also became clear that the integral-delay model has either to be modified to represent the details of all the QP mode of propagation for each R, or to be applied to all values of R together. These developments, as well as

the extension of the study to two-dimensional medium, open the door for interesting and challenging future work.

Appendix I: Methods to Solve the One-Dimensional Cable Equation with Discrete Gap Junction Resistance

To solve the Eq.(2.3), $K^2 = \frac{\rho SC}{\Delta t}$ and $g(x) = \rho S I_{ion}(x,t) - K^2 V(x, t - \Delta t)$, its solution can be expressed as the sum of a particular solution V_p^i and the homogeneous solution V_h^i ($V^i = V_p^i + V_h^i$), and here V_h^i is given by

$$V_h^i(x) = A^i e^{kx} + B^i e^{-kx}, \tag{1}$$

V_p^i is obtained by solving Eq.(2.3) with Neumann boundary condition ($\frac{\partial V_p^i}{\partial x}|_{x=0,L_c} = 0$) by the linear finite element method.

In using the finite element method, we divide one cell to N segments by $N+1$ nodes, as shown by the Fig. 1. The conditions at the beginning and the end of the cell are given by $\frac{\partial V_p^i}{\partial x}|_{x=0,L_c} = 0$.

Let us consider the function $L(V)$ which is given by the difference between the left and right sides of Eq.(2.3)

$$L(V) = \frac{\partial^2 V(x,t)}{\partial x^2} - K^2 V(x,t) - g(x,t). \tag{2}$$

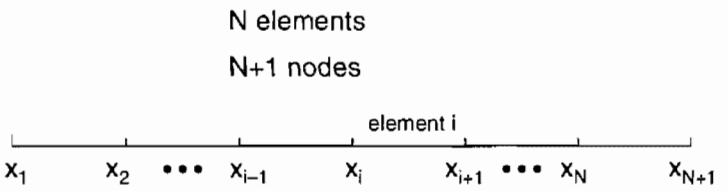

Figure 1: The schema of N elements.

We use the finite element method, and the weight function $n_i(x)$ for the ith node is given by

$$n_i(x) = \begin{cases} 0 & x < x_{i-1} \\ \frac{x-x_{i-1}}{x_i-x_{i-1}} & x_{i-1} \leq x < x_i \\ \frac{x_{i+1}-x}{x_{i+1}-x_i} & x_i \leq x < x_{i+1} \\ 0 & x \geq x_{i+1} \end{cases} \tag{3}$$

Let us take the fixed time t, the potential being only the function of the space x that is given by $V(x)$, it is rewritten by the term of the potential V_p^i and the weight functions $n_i(x)$ for the node i

$$V(x) = n_{i-1}V_p^{i-1} + n_iV_p^i + n_{i+1}V_p^{i+1} \tag{4}$$

where x is in the interval $[x_{i-1}^+, x_{i+1}^-]$. For $i = 1, 2 \ldots N$, combine Eq.(2) and Eq.(4) to define the function χ it is given by $\chi_i = \int_{i\ node} n_i(x)L(V)dl = \int_{x_{i-1}^+}^{x_{i+1}^-} n_i(x)L(V)dx = A + B + C = 0$ for any i node, here A, B and C are given by

$$A = \int_{x_{i-1}^+}^{x_{i+1}^-} n_i(x)\frac{d^2V(x)}{dx^2}dx \tag{5}$$

$$B = -K^2\int_{x_{i-1}^+}^{x_{i+1}^-} n_i(x)V(x)dx \tag{6}$$

$$C = -\int_{x_{i-1}^+}^{x_{i+1}^-} n_i(x)g(x)dx. \tag{7}$$

1 Calculation of terms A, B and C

Let us integrate the term A,

$$A = \int_{x_{i-1}^+}^{x_{i+1}^-} n_i(x)\frac{d^2V(x)}{dx^2}dx = [n_i\frac{dV}{dx}]_{x_{i-1}^+}^{x_i^-} + [n_i\frac{dV}{dx}]_{x_i^+}^{x_{i+1}^-} - \int_{x_{i-1}^+}^{x_i^-}\frac{dn_i}{dx}\frac{dV}{dx}dx - \int_{x_i^+}^{x_{i+1}^-}\frac{dn_i}{dx}\frac{dV}{dx}dx \tag{8}$$

using the Eq.(3) and letting $\Delta x = x_{i+1}^- - x_i^+ = x_i^- - x_{i-1}^+$, $V(x_i^+) = V(x_i^-) = V_p^i$, and $\frac{dV}{dx}|_{x_i^-} = \frac{dV}{dx}|_{x_i^+}$, we get A that is given by

$$A = \frac{1}{\Delta x}(V_p^{i-1} - 2V_p^i + V_p^{i+1}) \tag{9}$$

Use the same method, and B is given by

$$B = -K^2\int_{x_{i-1}^+}^{x_{i+1}^-} n_i(x)V(x)dx = -K^2[V_p^{i-1}\int_{x_{i-1}^+}^{x_i^-} n_i(x)n_{i-1}(x)dx + V_p^i\int_{x_{i-1}^+}^{x_i^-} n_i(x)n_i(x)dx$$

$$+ \quad V_p^i \int_{x_i^+}^{x_{i+1}^-} n_i(x)n_i(x)dx + +V_p^{i+1} \int_{x_i^+}^{x_{i+1}^-} n_i(x)n_{i+1}(x)dx] \tag{10}$$
$$= \quad -K^2\Delta x[\frac{1}{6}V_p^{i-1} + \frac{2}{3}V_p^i + \frac{1}{6}V_p^{i+1}]$$

The fraction is written by $g(x) = n_{i-1}(x)g_{i-1}(x) + n_i(x)g_i(x) + n_{i+1}g_{i+1}(x)$, and C term is calculated by

$$C = -\int_{x_{i-1}^+}^{x_{i+1}^-} n_i(x)g(x)dx = -\int_{x_{i-1}^+}^{x_i^-} n_i n_{i-1}g_{i-1}(x)dx - \int_{x_{i-1}^+}^{x_i^-} n_i n_i g_i(x)dx$$
$$- \int_{x_i^+}^{x_{i+1}^-} n_i g_i(x)dx - \int_{x_i^+}^{x_{i+1}^-} n_{i+1}g_{i+1}(x)dx \tag{11}$$
$$= -\Delta x[\frac{1}{6}g_{i-1}(x) + \frac{2}{3}g_i(x) + \frac{1}{6}g_{i+1}] \tag{12}$$

For the first node ($i = 1$) and the last node ($i = N + 1$), with the relations $V(x_{i-1}^+) = V(x_i^-) = 0$ and $V(x_i^+) = V(x_{i+1}^-) = 0$, A^1, B^1, C^1, A^N, B^N and C^N are given by

$$A^1 = \frac{1}{\Delta x}(V_p^2 - V_p^1) \tag{13}$$
$$B^1 = -K^2\Delta x[\frac{1}{3}V_p^1 + \frac{1}{6}V_p^2] \tag{14}$$
$$C^1 = -\Delta x[\frac{1}{3}g_1 + \frac{1}{6}g_2] \tag{15}$$
$$A^N = \frac{1}{\Delta x}(V_p^N - V_p^{N+1}) \tag{16}$$
$$B^N = -K^2\Delta x[\frac{1}{6}V_p^N + \frac{1}{3}V_p^{N+1}] \tag{17}$$
$$C^N = -\Delta x[\frac{1}{6}g_N + \frac{1}{3}g_{N+1}], \tag{18}$$

then the first term (χ_1) obtains

$$\chi_1 = \frac{1}{\Delta x}[-1 \;\; 1][\begin{matrix}V_p^1\\V_p^2\end{matrix}] - K^2\Delta x[1/3 \;\; 1/6][\begin{matrix}V_p^1\\V_p^2\end{matrix}] - \Delta x[1/3 \;\; 1/6][\begin{matrix}g_1\\g_2\end{matrix}] = 0 \tag{19}$$

$$[(-\frac{1}{(\Delta xK)^2} - \frac{1}{3}) \;\; (\frac{1}{(\Delta xK)^2} - \frac{1}{6})][\begin{matrix}V_p^1\\V_p^2\end{matrix}] = \frac{1}{K^2}[1/3 \;\; 1/6][\begin{matrix}g_1\\g_2\end{matrix}]. \tag{20}$$

Let us put $Q = \frac{1}{(\Delta xK)^2}$, Eq.(20) is rewritten by

$$[(-Q - \frac{1}{3}) \;\; (Q - \frac{1}{6})][\begin{matrix}V_p^1\\V_p^2\end{matrix}] = \frac{1}{K^2}[1/3 \;\; 1/6][\begin{matrix}g_1\\g_2\end{matrix}], \tag{21}$$

for the last term of the node $N+1$ (χ_{N+1}), the relation yield below,

$$[(Q-\frac{1}{6})\ (-Q-\frac{1}{3})][\begin{matrix}V_p^N\\V_p^{N+1}\end{matrix}]=\frac{1}{K^2}[1/6\ \ 1/3][\begin{matrix}g_N\\g_{N+1}\end{matrix}], \tag{22}$$

for the node $i=2,3,\cdots N$, they are given by

$$((Q-\frac{1}{6})\ (-2Q-\frac{2}{3})\ (Q-\frac{1}{6}))\begin{pmatrix}V_p^{i-1}\\V_p^i\\V_p^{i+1}\end{pmatrix}=\frac{1}{K^2}[\frac{1}{6}g_{i-1}+\frac{2}{3}g_i+\frac{1}{6}g_{i+1}]$$

Combine the $N+1$ equations as a matrix equation, it is given by

$$\begin{pmatrix}\alpha/2 & \beta & 0 & 0 & \cdots & 0\\ \beta & \alpha & \beta & 0 & \cdots & 0\\ 0 & \beta & \alpha & \beta & \cdots & 0\\ \vdots & \vdots & \ddots & \ddots & \ddots & \vdots\\ 0 & 0 & 0 & \beta & \alpha & \beta\\ 0 & 0 & 0 & 0 & \beta & \alpha/2\end{pmatrix}\begin{pmatrix}V_p^1\\V_p^2\\V_p^3\\\vdots\\V_p^N\\V_p^{N+1}\end{pmatrix}=\begin{pmatrix}h_1\\h_2\\h_3\\\vdots\\h_N\\h_{N+1}\end{pmatrix},$$

here $\alpha=-2(Q+\frac{1}{3})$, $\beta=Q-\frac{1}{6}$ and

$$h_i=\frac{1}{6K^2}\begin{cases}2g_1+g_2 & if \quad i=1\\ g_{i-1}+4g_i+g_{i+1} & if \quad 1<i<N\\ g_N+2g_{N+1} & if \quad i=N+1\end{cases}.$$

Let a matrix M is

$$M=\begin{pmatrix}\alpha/2 & \beta & 0 & 0 & \cdots & 0\\ \beta & \alpha & \beta & 0 & \cdots & 0\\ 0 & \beta & \alpha & \beta & \cdots & 0\\ \vdots & \vdots & \ddots & \ddots & \ddots & \vdots\\ 0 & 0 & 0 & \beta & \alpha & \beta\\ 0 & 0 & 0 & 0 & \beta & \alpha/2\end{pmatrix}.$$

2 Solution of V_p^i

To solve V_p^i, we decompose the matrix M to LU,

$$Mv=LUv=h. \tag{23}$$

The matrix M can be broken up into two triangular system matrices, let $Ly=h$ and $y=Uv$, the matrix L is the triangular below part, and U is the triangular above part with 1 on all the diagonal.

The matrices L and U are described below, the elements of the matrix of L are given by

$$l_{i,j} = \begin{cases} \alpha/2 & \text{i=j=1} \\ \beta & \text{i=j+1} \\ \alpha - \frac{\beta^2}{l_{i-1,j-1}} & i = j \neq 1, i = j \neq N+1 \\ \frac{\alpha}{2} - \frac{\beta^2}{l_{n,n}} & \text{i=j=N+1} \\ 0 & other \end{cases},$$

and the element of the matrix of U is given by

$$U_{i,j} = \begin{cases} 1 & i = j \\ \frac{\beta}{l_{i,j}} & j = i+1 \\ 0 & other \end{cases}$$

From $Ly = h$, the elements of the vector y is given by

$$y_i = \begin{cases} \frac{h_1}{l_{1,1}} & i = 1 \\ \frac{h_i - \beta y_{i-1}}{l_{i,i}} & i > 1 \end{cases}$$

We know the triangular above part matrix is given by $Uv = y$, therefore the elements of the vector v is given by

$$V_p^i = \begin{cases} y_{N+1} & i = N+1 \\ y_i - \frac{\beta}{l_{i,i}} V_p^{i+1} & i < N+1 \end{cases}$$

3 Connection the Cell

Once the particular solution of potential V_p^i is obtained, we connect all cells to fulfill the boundary conditions Eq.(2.2), using the constants A^i and B^i of the homogeneous solution. For cell $i = 1, 2 \cdots n-1$ (n: the number of cell), the two boundary conditions can be expressed as:

$$\begin{aligned} V_p^i(L_c) + A^i e^{KL_c} + B^i e^{-KL_c} &= V_p^{i+1}(0) + A^{i+1} + B^{i+1} - \frac{\pi a^2 R}{\rho}[A^i K e^{KL_c} - B^i K e^{-KL_c}] \\ A^i K e^{KL_c} - B^i K e^{-KL_c} &= A^{i+1} K - B^{i+1} K \end{aligned} \quad (24)$$

For $i = n$, boundary conditions are given by

$$\begin{aligned} V_p^n(L_c) + A^n e^{KL_c} + B^n e^{-KL_c} &= V_p^1(0) + A^1 + B^1 - \frac{\pi a^2 R}{\rho}[A^n K e^{KL_c} - B^n K e^{-KL_c}] \\ A^n K e^{KL_c} - B^n K e^{-KL_c} &= A^1 K - B^1 K \end{aligned} \quad (25)$$

Let $\beta = \frac{R\pi a^2 K}{\rho}$, $\zeta = e^{KL_c}$ and $G^i = V_p^{(mod(i,n)+1)}(0) - V_p^i(L_c)$. Combining the Eq.(24) and Eq.(25), the $2n$ equations can be rewritten as $Mx = y$, where the matrix M, the vector x and y are given by these three equations below, respectively.

$$M = \begin{pmatrix} \zeta(1+\beta) & -1 & \cdot & 0 & 0 & \frac{(1-\beta)}{\zeta} & -1 & \cdot & 0 & 0 \\ 0 & \zeta(1+\beta) & \cdot & 0 & 0 & 0 & \frac{(1-\beta)}{\zeta} & \cdot & 0 & 0 \\ \vdots & \vdots & \vdots & \vdots & \vdots & \vdots & \vdots & \vdots & \vdots & \vdots \\ 0 & 0 & \cdot & \zeta(1+\beta) & -1 & 0 & 0 & \cdot & \frac{(1-\beta)}{\zeta} & -1 \\ -1 & 0 & \cdot & 0 & \zeta(1+\beta) & -1 & 0 & \cdot & 0 & \frac{(1-\beta)}{\zeta} \\ \zeta K & -K & \cdot & 0 & 0 & -\frac{K}{\zeta} & K & \cdot & 0 & 0 \\ 0 & \zeta K & \cdot & 0 & 0 & 0 & -\frac{K}{\zeta} & \cdot & 0 & 0 \\ \vdots & \vdots & \vdots & \vdots & \vdots & \vdots & \vdots & \vdots & \vdots & \vdots \\ 0 & 0 & \cdot & \zeta K & -K & 0 & 0 & \cdot & -\frac{K}{\zeta} & K \\ -K & 0 & \cdot & 0 & \zeta K & K & 0 & \cdot & 0 & -\frac{K}{\zeta} \end{pmatrix} \tag{26}$$

$$x = \begin{pmatrix} A^1 \\ A^2 \\ \vdots \\ A^{n-1} \\ A^n \\ B^1 \\ B^2 \\ \vdots \\ B^{n-1} \\ B^n \end{pmatrix} \tag{27}$$

$$y = \begin{pmatrix} G^1 \\ G^2 \\ \vdots \\ G^{n-1} \\ G^n \\ 0 \\ 0 \\ \vdots \\ 0 \\ 0 \end{pmatrix} \tag{28}$$

To obtain A^i and B^i, we need to compute the inverse matrix of M^{-1}. For solving M^{-1}, consider an $n \times n$ permutation matrix P given by

$$P = \begin{pmatrix} 0 & 1 & 0 & \cdots & 0 \\ 0 & 0 & 1 & \cdots & 0 \\ \vdots & \ddots & \ddots & \ddots & \vdots \\ 1 & 0 & 0 & \cdots & 0 \end{pmatrix}.$$

The matrix P has specific characteristics. If P multiplies any matrix T from left $(P \cdot T)$, the result is a circular permutation of the row of T, the direction of the rotation is from top to bottom. For example, if T is given by

$$T = \begin{pmatrix} T_{1,1} & T_{1,2} & \cdots & T_{1,n} \\ T_{2,1} & T_{2,2} & \cdots & T_{2,n} \\ \vdots & \ddots & \ddots & \vdots \\ T_{n-1,1} & T_{n-1,2} & \cdots & T_{n-1,n} \\ T_{n,1} & T_{n,2} & \cdots & T_{n,n} \end{pmatrix},$$

then, $P \cdot T$ is:

$$P \cdot T = \begin{pmatrix} T_{2,1} & T_{2,2} & \cdots & T_{2,n} \\ T_{3,1} & T_{3,2} & \cdots & T_{3,n} \\ \vdots & \ddots & \ddots & \vdots \\ T_{n,1} & T_{n,2} & \cdots & T_{n,n} \\ T_{1,1} & T_{1,2} & \cdots & T_{1,n} \end{pmatrix},$$

The first row of T becomes the last row of $P \cdot T$, and all the other rows decrease and are pushed upward.

When P multiplies any matrix T from right $(T \cdot P)$, the resulting matrix is a circular permutation of the column of T. The direction of rotation is from right to left. For example, multiplying T given by above P gives:

$$T \cdot P = \begin{pmatrix} T_{1,n} & T_{1,1} & \cdots & T_{1,n-1} \\ T_{2,n} & T_{2,1} & \cdots & T_{2,n-1} \\ \vdots & \ddots & \ddots & \vdots \\ T_{n-1,n} & T_{n-1,1} & \cdots & T_{n-1,n-1} \\ T_{n,n} & T_{n,1} & \cdots & T_{n,n-1} \end{pmatrix}.$$

The last column of T becomes the first column of $T \cdot P$, and all the other columns are shifted to the right. For P^2, P^3 and P^n, the matrix T is rotated two times, three times, until $(P^n = I)$, respectively.

The $2n \times 2n$ matrix M can be rewritten as:

$$M = \begin{pmatrix} (1+\beta)\zeta I - P & \frac{(1-\beta)}{\zeta} I - P \\ \\ K\zeta I - KP & -\frac{K}{\zeta} I + KP \end{pmatrix},$$

Defining the $2n \times 2n$ diagonal matrix J as:

$$J = \begin{pmatrix} 1 & 0 & \cdots & 0 & 0 & 0 & \cdots & 0 \\ 0 & 1 & \cdots & 0 & 0 & 0 & \cdots & 0 \\ \vdots & \ddots & \ddots & \ddots & \ddots & \ddots & \ddots & \vdots \\ 0 & 0 & \cdots & 1 & 0 & 0 & \cdots & 0 \\ 0 & 0 & \cdots & 0 & K & 0 & \cdots & 0 \\ 0 & 0 & \cdots & 0 & 0 & K & \cdots & 0 \\ \vdots & \ddots & \ddots & \ddots & \ddots & \ddots & \ddots & \vdots \\ 0 & 0 & \cdots & 0 & 0 & 0 & \cdots & K \end{pmatrix}$$

The matrix M can be rewritten

$$M = Jm \tag{29}$$

with m given by:

$$m = \begin{pmatrix} (1+\beta)\zeta I - P & \frac{(1-\beta)}{\zeta} I - P \\ \\ \zeta I - P & -\frac{1}{\zeta} I + P \end{pmatrix},$$

The inverse matrix M^{-1} then becomes:

$$M^{-1} = m^{-1} J^{-1} \tag{30}$$

The inverse matrix J^{-1} is:

$$J^{-1} = \begin{pmatrix} 1 & 0 & \cdots & 0 & 0 & 0 & \cdots & 0 \\ 0 & 1 & \cdots & 0 & 0 & 0 & \cdots & 0 \\ \vdots & \ddots & \ddots & \ddots & \ddots & \ddots & \ddots & \vdots \\ 0 & 0 & \cdots & 1 & 0 & 0 & \cdots & 0 \\ 0 & 0 & \cdots & 0 & \frac{1}{K} & 0 & \cdots & 0 \\ 0 & 0 & \cdots & 0 & 0 & \frac{1}{K} & \cdots & 0 \\ \vdots & \ddots & \ddots & \ddots & \ddots & \ddots & \ddots & \vdots \\ 0 & 0 & \cdots & 0 & 0 & 0 & \cdots & \frac{1}{K} \end{pmatrix},$$

The matrix m can be divided in four blocks

$$m = \begin{pmatrix} A & B \\ C & D \end{pmatrix},$$

where A, B, C and D are bidiagonal $n \times n$ matrices, they are given by

$$A = \begin{pmatrix} \zeta(1+\beta) & -1 & 0 & \cdots & 0 \\ 0 & \zeta(1+\beta) & -1 & \cdots & 0 \\ \vdots & \ddots & \ddots & \ddots & \vdots \\ -1 & 0 & 0 & \cdots & \zeta(1+\beta) \end{pmatrix} = \zeta(1+\beta)I - P,$$

$$B = \begin{pmatrix} \zeta^{-1}(1-\beta) & -1 & 0 & \cdots & 0 \\ 0 & \zeta^{-1}(1-\beta) & -1 & \cdots & 0 \\ \vdots & \ddots & \ddots & \ddots & \vdots \\ -1 & 0 & 0 & \cdots & \zeta^{-1}(1-\beta) \end{pmatrix} = \frac{(1-\beta)}{\zeta} I - P,$$

$$C = \begin{pmatrix} \zeta & -1 & 0 & \cdots & 0 \\ 0 & \zeta & -1 & \cdots & 0 \\ \vdots & \ddots & \ddots & \ddots & \vdots \\ -1 & 0 & 0 & \cdots & \zeta \end{pmatrix} = \zeta I - P,$$

$$D = \begin{pmatrix} -1/\zeta & 1 & 0 & \cdots & 0 \\ 0 & -1/\zeta & 1 & \cdots & 0 \\ \vdots & \ddots & \ddots & \ddots & \vdots \\ 1 & 0 & 0 & \cdots & -1/\zeta \end{pmatrix} = -\frac{I}{\zeta} + P,$$

If the inverse matrix m^{-1} can also be divided in four blocks:

$$m^{-1} = \begin{pmatrix} F & G \\ H & I \end{pmatrix},$$

The elements of the matrices A, B, C and D can be represented by using the permutation matrix. For example, the ith column of the matrix A is defined by the vector A_i:

$$A_i = \begin{pmatrix} a_{1,i} \\ a_{2,i} \\ \vdots \\ a_{n-1,i} \\ a_{n,i} \end{pmatrix}$$

Then (i+1)th column of A, A_{i+1} is given by

$$A_{i+1} = PA_i = P^i A_1, \qquad i = 1, 2, \cdots n-1 \tag{31}$$

When the permutation matrix P multiplies a matrix from the right, the same rule shown above can be used. For the inverse matrix m^{-1}, the first row of $m^{-1}m$ are given by Eq.(32) and Eq.(33)

$$\sum_i F_{1,i} A_{i,1} + G_{1,i} C_{i,1} = 1 \tag{32}$$

$$\sum_i F_{1,i}A_{i,j} + G_{1,i}C_{i,j} = 0, \qquad (j \neq 1) \tag{33}$$

Similarly, for the second row of $m^{-1}m$, the second element is 1 and the other are zero. Using the Eq.(31), these elements yield:

$$\sum_i F_{2,i}A_{i,2} + G_{2,i}C_{i,2} = \sum_i F_{2,i}PA_{i,1} + G_{2,i}PC_{i,1} = 1, \tag{34}$$

$$\sum_i F_{2,i}A_{i,j} + G_{2,i}C_{i,j} = \sum_i F_{2,i}PA_{i,j-1} + G_{2,i}PC_{i,j-1} = 0, \qquad (j \neq 2) \tag{35}$$

If $F_{1,i} = F_{2,i}P$ and $G_{1,i} = G_{2,i}P$, these relations are identical to Eq.(32) and Eq.(33). These operations can be repeated for rows in F and G. Therefore all the rows or columns of matrices F and G can be obtained by the circular permutation of the first row or column. We just have to find all elements of the first row, and the other $n-1$ rows can be obtained by permutation. By the same method, the matrices H and I can be proven to be circular, such that we only have to calculate all elements of a row or column of matrix.

We represent the first row m^{-1} by two $(n \times 1)$ vectors V and W, and compute the first line of $m^{-1}m$ to obtain:

$$(1+\beta)\zeta V - VP + \zeta W - WP = I_1 \tag{36}$$

$$\frac{(1-\beta)}{\zeta}V - VP - \frac{W}{\zeta} + WP = 0 \tag{37}$$

where I_1 is the first line of the $n \times n$ unit matrix. This yields:

$$\begin{aligned} & \left(\frac{\zeta^2(1+\beta)+(1-\beta)}{\zeta}\right)V - 2VP + \left(\frac{\zeta^2-1}{\zeta}\right)W = I_1 \Rightarrow \\ W &= \left(\frac{\zeta}{\zeta^2-1}\right)I_1 - \left(\frac{\zeta^2(1+\beta)+(1-\beta)}{\zeta^2-1}\right)V + \left(\frac{2\zeta}{\zeta^2-1}\right)VP \\ V &- \frac{2(\zeta^2+1)+\beta(\zeta^2-1)}{2\zeta}VP + VP^2 = \frac{1}{2\zeta}I_1 - \frac{1}{2}I_1P \end{aligned}$$

$$\begin{pmatrix} 1 & 0 & 0 & \cdots & 0 & 1 & -\frac{2(\zeta^2+1)+\beta(\zeta^2-1)}{2\zeta} \\ -\frac{2(\zeta^2+1)+\beta(\zeta^2-1)}{2\zeta} & 1 & 0 & \cdots & 0 & 0 & 1 \\ 1 & -\frac{2(\zeta^2+1)+\beta(\zeta^2-1)}{2\zeta} & 1 & \cdots & 0 & 0 & 0 \\ \vdots & \ddots & \ddots & \cdots & \ddots & \ddots & \vdots \\ 0 & 0 & 0 & \cdots & 1 & -\frac{2(\zeta^2+1)+\beta(\zeta^2-1)}{2\zeta} & 1 \end{pmatrix}$$

$$\begin{pmatrix} V_1 \\ V_2 \\ V_3 \\ \vdots \\ V_n \end{pmatrix} = \begin{pmatrix} \frac{1}{2\zeta} \\ -\frac{1}{2} \\ 0 \\ \vdots \\ 0 \end{pmatrix} \tag{38}$$

Similarly, representing the $(n+1)$th row of m^{-1} by two $(n \times 1)$ vectors X and Y, and computing the $(n+1)$th line of $m^{-1}m$ to obtain:

$$(1+\beta)\zeta X - XP + \zeta Y - YP = 0 \tag{39}$$

$$\frac{(1-\beta)}{\zeta}X - XP - \frac{Y}{\zeta} + YP = I_1 \tag{40}$$

$$\begin{aligned} & \frac{\zeta^2(1+\beta)+(1-\beta)}{\zeta})X - 2XP + (\frac{\zeta^2-1}{\zeta})Y = I_1 \Rightarrow \\ Y &= (\frac{\zeta}{\zeta^2-1})I_1 - (\frac{\zeta^2(1+\beta)+(1-\beta)}{\zeta^2-1})X + (\frac{2\zeta}{\zeta^2-1})XP \\ X &- \frac{2(\zeta^2+1)+\beta(\zeta^2-1)}{2\zeta}XP + XP^2 = \frac{\zeta}{2}I_1 - \frac{1}{2}I_1P \end{aligned}$$

Such that the final system for X is

$$\begin{pmatrix} 1 & 0 & 0 & \cdots & 0 & 1 & -\frac{2(\zeta^2+1)+\beta(\zeta^2-1)}{2\zeta} \\ -\frac{2(\zeta^2+1)+\beta(\zeta^2-1)}{2\zeta} & 1 & 0 & \cdots & 0 & 0 & 1 \\ 1 & -\frac{2(\zeta^2+1)+\beta(\zeta^2-1)}{2\zeta} & 1 & \cdots & 0 & 0 & 0 \\ \vdots & \ddots & \ddots & \cdots & \ddots & \ddots & \vdots \\ 0 & 0 & 0 & \cdots & 1 & -\frac{2(\zeta^2+1)+\beta(\zeta^2-1)}{2\zeta} & 1 \end{pmatrix}$$

$$\begin{pmatrix} X_1 \\ X_2 \\ X_3 \\ \vdots \\ X_n \end{pmatrix} = \begin{pmatrix} \frac{\zeta}{2} \\ -\frac{1}{2} \\ 0 \\ \vdots \\ 0 \end{pmatrix} \tag{41}$$

With these relations, m^{-1} can be obtained for each loop holding n cells. Then, for each time step, the appropriate values of A^i and B^i are obtained by performing the product $m^{-1}J^{-1}y$, with y given by Eq.(28). Because the last n rows are 0, only the values of the vectors V and X need to be computed. Besides, the non-zero first n elements of y correspond

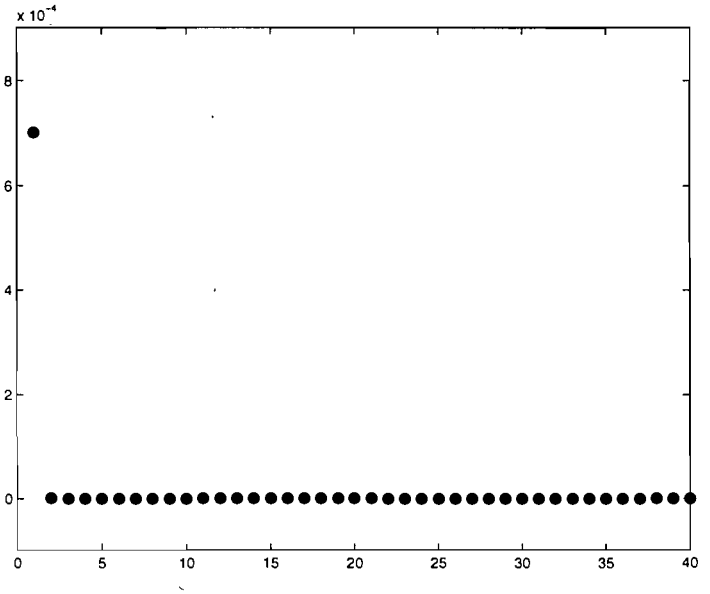

Figure 2: The 40 elements of V.

to the difference of potential between the end of a cell and the beginning of its first right neighbors, which permits a further simplification of the calculation, as explained below.

In our model, the parameters of the cable are $\rho = 0.2K\Omega cm$, $S = 4000cm^{-1}$, $C_m = 1\mu Fcm^{-2}$, $\Delta t = 0.002ms$, such that $K = \sqrt{\frac{\rho SC}{\Delta t}} = 632.4555cm^{-1}$. We have chosen to perform the simulations with a precision of 10^{-5}mV for potential V. Since the length of cell is $L_c = 100\mu m$, $e^{KL_c} = 558.1094$.

We considered that a loop has 40 cells with a gap resistance of $R = 100\Omega$, the elements of the vectors V and X, solutions of the equations (38) and (41) then getting the results of A^i and B^i, are shown on Fig. 2 and Fig. 3. The elements of V beyond those of the first neighbors are to the order of 10^{-9}. If the maximum difference of potential between the cells is to the order of $10mV$ and $\zeta = e^{KL_c}$ is to the order of 10^2 , the contribution $A^i e^{KL_c}$ of the second neighbours to the potential of the center cell will be to the order of $10^{-6}mV$, which can be neglected. Similarly, the contribution of the second neigbours for X will be to the order of 10^{-7}, if the maximum difference of action potential between the nearest nodes is less than $10mV$ and e^{-K0} given by 1, the potential B^i is around $10^{-6}mV$, and it can

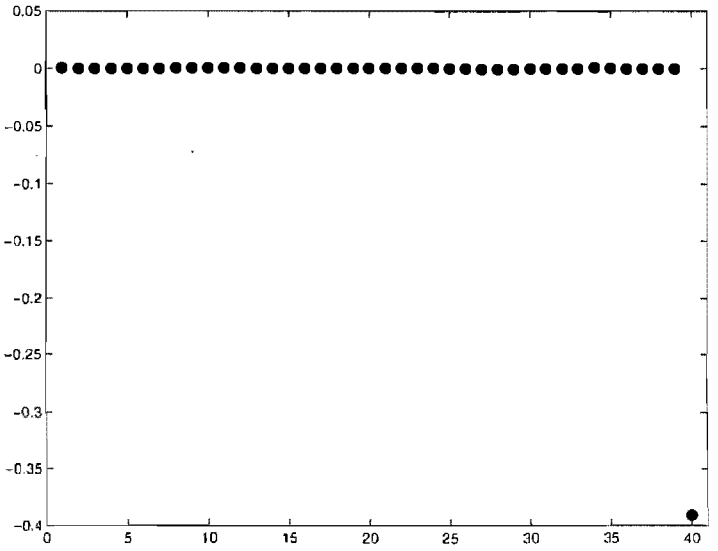

Figure 3: The 40 elements of X.

be ignored. Therefore, in this case, it is sufficient to keep only the contribution of the first neighbours for calculation of the potential, which simplifies and speeds up the calculation. This approximation becomes even better as R is increased.

Bibliography

[1] http://www40.statcan.ca/l01/cst01/health30a.htm?sdi=death%20disease(Mar. 21,2007).

[2] http://www.census.gov/compendia/statab/tables/07s0108.xls (Mar. 21,2007).

[3] http://research.medicine.wustl.edu/OCFR/Research.nsf/Abstracts/CD1761F8EFC 7893286257038006803 50?OpenDocument&VW=Imaging (Mar. 21,2007).

[4] http://www.cvphysiology.com/Arrhythmias/A008c.htm (Mar. 21,2007).

[5] L. Boersma, J. Brugada, C. J. H. Kirchhof and M. A. Allessie: Entrainment of reentrant ventricular tachycardia in anisotropic rings of rabbit myocardium. Mechanisms of termination, changes in morphology, and acceleration. Circulation **88**, 1852-1865 (1993).

[6] J. Brugada, L. Boersma, C. J. H. Kirchhof V. V. T. Heyenen and M. A. Allessie: Reentrant excitation around a fixed obstacle in uniform anisotropic ventricular myocardium. Circulation **84**, 1296-1306 (1991).

[7] P. L. Rensma, M. A. Allessie, W. J. E. P. Lammers, F. I. M. Bonke and M. J. Schalij: Length of excitation wave and susceptibility to reentrant atrial arrhythmias in normal conscious dogs. Circ. Res. **62**, 395-410 (1988).

[8] L. H. Frame and M. B. Simson: Oscillations of conduction, action potential duration, and refractoriness. A mechanism for spontaneous termination of reentrant tachycardias. Circulation **78**, 1277-1287 (1988).

[9] R. M. Berne, M. N. Levy: Cardiovascular Physiology, Eighth Edition, Mosby Inc. (2001).

[10] A. C. Guyton: Textbook of Medical Physiology, W. S. Saunders, (1991).

[11] S. I. Fox: Human Physiology, Eighth Edition, WCB/McGraw-Hill, (2001).

[12] R. H. Helfant: Bellet's Essential of Cardiac Arrhythmias, Philadelphia: Saunder, (1980).

[13] http://medical-dictionary.thefreedictionary.com/atrioventricular+(AV)+junctional+escape +rhythm (Mar. 22, 2007).

[14] L. H. Frame, R. L. Page, P. A. Boyden, J. J. Fenoglio and B. F. Hoffman: Circus movement in the canine atrium around the tricuspid ring during experimental atrial flutter and during reentry in vitro. Circulation, **76**, 1155-1187 (1987).

[15] R. C. Bernstein and L. H. Frame: Ventricular reentry around a fixed barrier. Resetting with advancement in an in vitro model. Circulation **81**, 267-280 (1990).

[16] S. Cardin, E. Libby, P. Pelletier, S. L. Bouter, A. S. Takeshita, N. L. Meur, J. Léger, S. Demolombe, A. Ponton, L. Glass, and S. Nattel: Contrasting Gene Expression Profiles in Two Canine Models of Atrial Fibrillation. Circ. Res. **100**, 425-433 (2007).

[17] G. M. Faber and Y. Rudy: Action potential and contractillity changes in $[Na^+]_i$ overloaded cardiac myocytes. Biophys. J. **78**, 2392-2404 (2000).

[18] G. W. Beeler and H. Reuter: Reconstruction of the action potential of ventricular myocardial fibres. J. Physiol. **268**, 177-210 (1977).

[19] A. L. Hodgkin and A. F. Huxley: A Quantitative description of membrane current and its application to conduction and excitation. Nerve. J. Physiol. **117**, 500-544 (1952).

[20] J. P. Drouhard and F. A. Roberge: Revised formulation of the Hodgkin-Huxley representation of the sodium current in cardiac cells. Comput. Biomed. Res. **20**, 333-350 (1987).

[21] R. M. Gulrajani: Bioelectricity and Biomagnetism, J. Wiley, (1998).

[22] S. W. Kuffler, J. G. Nicholls and Q. R. Martin: From Neuron to Brain, second edition, Sunderland, Massachusetts, (1984).

[23] A Vinet and F. A. Roberge: A model study of stability and oscillations in the myocardial cell membrane. J. Theor. Biol. **147**, 377-412 (1990).

[24] A. Vinet, D. R. Chialvo, D. C. Michaels and J. Jalife: Non-linear dynamics of rate-dependent activation in models of single cardiac cells. Circ. Res. **67**, 1510-1524 (1990).

[25] A Vinet: Memory and bistability in a one-dimensional loop model of cardiac cell. J. Biol. System **7**, 451-473 (1999).

[26] A Vinet and Y. Henzel: Dynamical Memory and its low dimensional representation in a model of cardiac myocytes. Phys. in Canada **57**, 129-136 (2001).

[27] A. Vinet and F. A. Roberge: The dynamics of sustained reentry in a ring model of cardiac tissue. Ann. Biomed. Eng. **22**, 568-591 (1994).

[28] A. Vinet and L. J. Leon: Circulation of activity in a loop of model myocardial cells. Proc. 13th IEEE/EMBC Conf. Orlando, FL. 508-509 (1991).

[29] A. Vinet: Quasi-Periodic Movement in a Ring Model of Cardiac Tissue: Mulit-Stability and Low Dimensional Equivalence. Ann. Biomed. Eng. **28**, 704-720 (2000).

[30] M. Courtemanche, L. Glass and J. P. Keener: Instabilities of a propagation pulse in a ring of excitable media. Phys. Rev. Lett. **70** , 2182-2185 (1993).

[31] M. Courtemanche, J. P. Keener and L. Glass: A Delay Equation Representation of Pulse Circulation on a Ring in Excitable Media. SIAM J. Appl. Math. **56**, 119-142 (1996).

[32] B. Echebarria and A. Karma: Instability and Spatiotemporal Dynamics of Alternans in Paced Cardiac Tissue. Phys. Rev. Let. **88**, 208101-4 (2002).

[33] A. Karma: Spiral breakup in model equations of action potential propagation in cardiac tissue. Phys. Rev. Lett. **71**, 1103-1106 (1993).

[34] T. J. Lewis and M. R. Guevara: Chaotic dynamics in an ionic model of the propagated cardiac action potential. J. Theoret. Biol. **146**, 407-432 (1990).

[35] W. Quan and Y. Rudy: Unidirectional block and reentry of cardiac excitation: A model study. Circ. Res. **66**, 367-382 (1990).

[36] X. Chen, F. H. Fenton and R. A. Gray: Head-tail interactions in numerical simulations of reentry in a ring of cardiac tissue. Heart Rhythm **2**, 1038-1046 (2005).

[37] P. Comtois and A. Vinet: Resetting and annihilation of reentrant activity in a model of a one-dimensional loop of ventricular tissue. Chaos **12**, 903-922 (2002).

[38] P. Comtois and A. Vinet: Stability and bifurcation in an integral-delay model of cardiac reentry including spatial coupling in repolarization. Phys. Rev. E, **68**, 051903-8 (2003).

[39] P. Comtois and A. Vinet: Multistability of reentrant rhythms in an ionic model of a two-dimensional annulus of cardiac tissue. Phys. Rev. E. **72**, 051927-11 (2005).

[40] P. Comtois and A. Vinet: Curvature effects on activation speed and repolarization in an ionic model of cardiac myocyte. Phys. Rev. E, **60**, 4619-4628 (1999).

[41] P. Comtois, A. Vinet and S. Nattel: Wave block formation in homogeneous excitable media following premature excitations: Dependence on restitution relations. Phys. Rev. E, **72**, 031919-5 (2005).

[42] N. F. Otani: A fast kinematic dynamo in 2-d time dependent flows, J. Fluid Mechanics **235**, 327-340 (1993).

[43] M. S. Spach, W. T. Miller, D. B. Geselowitz, R. C. Barr, J. M. Kootsey and E. A. Johnson: The discontinuous nature of propagation in normal canine cardiac muscle. Evidence for recurrent discontinuities of intracellular resistance that affect the membrane currents. Circ. Res. **48**, 39-54 (1981).

[44] M. S. Spach, J. F. Heidlage, P. C. Dolber and R. C. Barr: Electrophysiological Effects of Remodeling Cardiac Gap Junctions and Cell Size: Experimental and Model Studies of Normal Cardiac Growth. Circ. Res. **86**, 302-311 (2000).

[45] L. Zhang, K. Ina, H. Kitamura, G. R. Campbell and T. Shimada: The intercalated discs of monkey myocardial cells and Purkinje fibers as revealed by scanning electron microscopy. Arch. Histol. Cytol. **59**, 453-465 (1996).

[46] L. M. Davis, H. L. Kanter, E. C. Beyer and J. E. Saffitz: Distinct gap junction protein phenotypes in cardiac tissues with disparate conduction properties. J. Am. Coll Cardiol **24**, 1124-1132 (1994).

[47] J. E. Saffitz and M. Yeafer: Intracardiac cell communication and gap junctions. In: Foundation of Cardiac Arrhythmias, edited by Spooner P and Rosen M. New York: Dekker, 2000, 171.

[48] J. E. Saffitz, M. D. Loyd, B. J. Darrow H. L. Kanter J. G. Laing and E. C. Beyer: The molecular basis of anisotropy: rol of gap junctions. J Cardiovasc. J Cardiovasc. Electrophysiol. **6**, 498510 (1995).

[49] K. Willecke, J. Eiberger, J. Degen, D. Eckhardt, A. Romualdi, M. Guldenage, U. Deutsch and G. Sohl: Structural and functional diversity of connexin genes in the mouse and human genome. Biol. Chem. **383**, 725-737 (2002).

[50] W. H. Evans and P. E. M. Martin: Gap junctions: Structure and Function (Review) Mol. Membr. Biol. **19**, 121-136 (2002).

[51] R. Gourdie, C. Green, N. Severs and R. Thompson: Immunolabelling patterns of gap junction connexins in the developing and mature rat heart. Anat. Embryol **185**, 163-178 (1992).

[52] H. Kanter, J.Saffitz and E. Beyer: Cardiac myocytes express multiple gap junction proteins. Circ. Res. **70**, 438-444 (1992).

[53] P. W. Oosthoek, S. Viragh, W. H. Lamers, and A. F. Moorman: Immunohistochemical delineation of the conduction system. II. The atrioventricular node and Purkinje fibers. Circ. Res. **73**, 482-491 (1993).

[54] P. W. Oosthoek, S. Viragh, A. E. Mayen, M. J van Kempen, W. H. Lamers, and A. F. Moorman: Immunohistochemical delineation of the conduction system. I: The sinoatrial node. Circ. Res. **73**, 473-481 (1993).

[55] M. J van Kempen, C. Fromaget, D. Gros, A. F. Moorman, and W. H. Lamers: Spatial distribution of connexin43, the major cardiac gap junction protein, in the developing and adult rat heart. Circ. Res. **68**, 1638-1651 (1991).

[56] J. M. B. Anumonwo, H. Z. Wang, E. Trabka-Janik, B. Dunham, R. D. Veenstra, M. Delmar, and J. Jalife: Gap junctional channels in adult mammalian sinus nodal cells. Immunolocalization and electrophysiology. Circ. Res. **71**, 229-239 (1992).

[57] T. Opthof: Gap junctions in the sino-atrial node: immunohistochemical localization and correlation with activation pattern. J. Cardiovasc. Electrophysiol. **5**, 138-143 (1994).

[58] E. Trabka-Janik, W. Coombs, L. F. Lemanski, M. Delmar and J. Jalife: Immunohistochemical localization of gap junction protein channels in hamster sinoatrial node in

correlation with electrophysiologic mapping of the pacemaker region. J. Cardiovasc. Electrophysiol. **5**, 125-137 (1994).

[59] B. Bastide, L. Neyses, D. Ganten, M. Paul, K. Willecke, and O. Traub: Gap junction protein connexin40 is preferentially expressed in vascular endothelium and conductive bundles of rat myocardium and is increased under hypertensive conditions. Circ. Res. **73**, 1138-1149 (1993).

[60] S. Chen, L. M. Westphale, E. C. Beyer and J.E. Saffitz: Expression of multiple gap junction proteins in human fetal and infant heart. Pediatr. Res. **36**, 561-566 (1994).

[61] D. Gros, T. Jarry-Guichard, I. Ten Velde, A. de Maziere, M. J. van Kempen, J. Davoust, J. P. Briand, A. F. Moorman, and H. J. Jongsma: Restricted distribution of connexin40, a gap junctional protein, in mammalian heart. Circ. Res. **74**, 839-851 (1994).

[62] W. Schoels, H. Yang, W. B. Gough, and N. el-Sherif: Circus movement atrial flutter in the canine sterile pericarditis model. Differential effects of procainamide on the components of the reentrant pathway. Circ. Res. **68**, 1117-1126 (1991).

[63] F. F. Bukauskas, R. Vogel and R. Weingart: Biophysical properties of heterotypic gap junctions newly formed between two types of insect cells. J. Physiol. **499**, 701-713 (1997).

[64] G. T. Cottrell and J. M. Burt: Heterotypic gap junction channel formation between heteromeric and homomeric Cx40 and Cx43 connexins. Am J.Physiol. Cell. Physiol. **281**, C1559-C1567 (2001).

[65] D. S. He, J. X. Jiang S. M. Taffet and J. M. Burt: Formation of heteromeric gap junction channels by connexins 40 and 43 in vascular smoth muscle cells. Proc. Natl. Acad. Sci. USA. **96**, 6495-6500 (1999).

[66] D. I. Vaney and R. Weiler: Evidence for heteromeric, heterotypic and mixed-homotypic interactions. Brain Res. **32**, 115-120 (2000).

[67] L. Venance, J. Cordier M. Monge, B. Zalc, J. Glowinski and C. Giaume: Homotypic and heterotypic coupling mediated by gap junctions during glial cell differentiation in vitro. Eur. J. Neurosci. **7**, 451-461 (1995).

[68] A. G. Kléber and Y. Rudy: Basic Mechanisms of Cardiac Impulse Propagation and Associated Arrhythmias. Physiol. Rev. **84**, 431-488 (2004).

[69] J. P. Keener: The effects of discrete gap junction coupling on propagation in myocardium. J. Theor. Biol. **148**, 49-82 (1991).

[70] R. M. Shaw and Y. Rudy: Ionic Mechanisms of Propagation in Cardiac Tissue : Roles of the Sodium and L-type Calcium Currents During Reduced Excitability and Decreased Gap Junction Coupling. Circ. Res. **81**, 727-741 (1997).

[71] R. W. Joyner: Effects of the discrete pattern of electrical coupling on propagation through an electrical syncytium. Circ. Res. **50**, 192-200 (1982).

[72] I. Tasaki and S. Hagiwara: Capacity of Muscle Fiber Membrane. Am. J. Physiol. **188**, 423-429 (1957).

[73] Y. Rudy and W. L. Quan: A Model Study of the Effects of the discrete Cellular Structure on Electrical Propagation in Cardiac Tissue. Circ. Res. **61**, 815-823 (1987).

[74] R. M. Shaw and Y. Rudy: Electrophysiologic Effects of Acute Myocardial Ischemia: A Mechanistic Investigation of Action Potential Conduction and Conduction Failure. Circ. Res. **81**, 124-138 (1997).

[75] P. L. Rensma, M. A. Allessie, W. J. E. P. Lammers, F. I. M. Bonke and M. J. Schalij: Length of excitation wave and susceptibility to reentrant atrial arrhythmias in normal conscious dogs. Circ. Res. **62** , 395-410 (1988).

[76] E. Cytrynbaum and J. P. Keener: Stability conditions for the traveling pulse: Modifying the restitution hypothesis, Chaos **12**, 788-799 (2002).

[77] G. A. Gottwald and L. Kramer: A normal form for excitable media. Chaos **16**, 13122-10 (2006).

[78] M.S. Spach and J.F. Heidlage: The Stochastic Nature of Cardiac Propagation at a Microscopic Level : Electrical Description of Myocardial Architecture and Its Application to Conduction. Circ. Res. **76**, 366-380 (1995).

[79] Y. Rudy: Reentry: Insights from Theoretical Simulations in a Fixed Pathway. J. Cardiovasc. Electrophysiol. **6**, 294-312 (1995).

[80] V. G. Fast and A. G. Kléber: Microscopic conduction in cultured strands of neonatal rat heart cells measured with voltage-sensitive dyes. Circ. Res. **73**, 914-925 (1993).

[81] Y. Rudy and W. L. Quan: A model study of the effects of the discrete cellular structure on electrical propagation in cardiac tissue. Circ. Res. **61**, 815-823 (1987).

[82] F. A. Roberge, A. Vinet and B. Victorri: Reconstruction of propagated electrical activity with a two-dimensional model of anisotropic heart muscle. Circ. Res. **58**, 461-475 (1986).

[83] A. G. Kléber, C. B. Riegger and M. J. Janse: Electrical uncoupling and increase of extracellular resistance after induction of ischemia in isolated, arterially perfused rabbit papillary muscle. Circ. Res. **61**, 271-279 (1987).

[84] R. Jamaleddine and A. Vinet: Role of gap junction resistance in rate-induced delay in conduction in a cable model of the atrioventricular node. J. Biol. Sys. **7**, 475-499, (1999).

[85] A. P. Henriquez, R. Vogel, B. J. Muller-Borer, C. S. Henriquez, R. Weingart and W. E. Casio: Influence of Dynamic Gap Junction Resistance on Impulse Propagation in

Ventricular Myocardium: A Computer Simulation Study. Biophy. J. **81**, 2112-2121 (2001).

[86] C. Oka, H. Matsuda, N. Sarai and A. Noma: Modeling the calcium gate of cardiac gap junction channel. J. Physiol. Sci. **56**, 79-85 (2006).

[87] F. Xie, Z. Qu and A. Garfinkel: Dynamics of reentry around a circular obstacle in cardiac tissue. Phys. Rev. E **58**, 6355-6358 (1998).

[88] Z. Qu: Dynamical effects of diffusive cell coupling on cardiac excitation and propagation: a simulation study. Am. J. Physiol. **287**, H2803-H2812 (2004).

[89] Z. Qu and H. R. Karagueuzian, A. Garfinkel and J.N. Weiss: Effects of Na^+ channel and cell coupling abnormalities on vulnerability to reentry: a simulation study. Am. J. Physiol. **286**, H1310-H1321 (2004).

[90] E. M. Cherry and F. H. Fenton: Suppression of alternans and conduction blocks despite steep APD restitution: electrotonic, memory, and conduction velocity restitution effects. Am. J. Physiol. **286**, H2332-H2341 (2004).

[91] A. Vinet, D. R. Chialvo and J. Jalife: Irregular dynamics of excitation in biologic and mathematical models of cardiac cells. Ann. N.Y. Acad. Sci. **601** , 281-298 (1990).

[92] A. Vinet, D. R. Chialvo, D. C. Michaels and J. Jalife: Nonlinear dynamics of rate-dependent activation in models of single cardiac cells. Circ. Res. **67** , 1510-1524 (1990).